

# SPiRaL: a multiresolution global tomography model of seismic wave speeds and radial anisotropy variations in the crust and mantle

N.A. Simmons<sup>ID</sup>, S.C. Myers, C. Morency, A. Chiang and D.R. Knapp

Atmospheric, Earth and Energy Division, Lawrence Livermore National Laboratory, 7000 East Avenue, Livermore, CA 94550, USA.  
E-mail: [simmons27@llnl.gov](mailto:simmons27@llnl.gov)

Accepted 2021 July 16. Received 2021 June 25; in original form 2020 December 15

## SUMMARY

SPiRaL is a joint global-scale model of wave speeds ( $P$  and  $S$ ) and anisotropy (vertical transverse isotropy, VTI) variations in the crust and mantle. The model is comprised of >2.1 million nodes with five parameters at each node that capture velocity variations for  $P$ - and  $S$ -waves travelling at arbitrary directions in transversely isotropic media with a vertical symmetry axis (VTI). The crust (including ice, water, sediments and crystalline layers) is directly incorporated into the model. The default node spacing is approximately  $2^\circ$  in the lower mantle and  $1^\circ$  in the crust and upper mantle. The grid is refined with  $\sim 0.25^\circ$  minimum node spacing in highly sampled regions of the crust and upper mantle throughout North America and Eurasia. The data considered in the construction of SPiRaL includes millions of body wave traveltimes (crustal, regional and teleseismic phases with multiples) and surface wave (Rayleigh and Love) dispersion. A multiresolution inversion approach is employed to capture long-wavelength heterogeneities commonly depicted in global-scale tomography images as well as more localized details that are typically resolved in more focused regional-scale studies. Our previous work has demonstrated that such global-scale models with regional-scale detail can accurately predict both teleseismic and regional body wave traveltimes, which is necessary for more accurate location of small seismic events that may have limited signal at teleseismic distances. SPiRaL was constructed to predict traveltimes for event location and long-period waveform dispersion for seismic source inversion applications in regions without sufficiently tuned models. SPiRaL may also serve as a starting model for full-waveform inversion (FWI) with the goal of fitting waves with periods 10–50 s over multiple broad regions (thousands of kilometres) and potentially the globe. To gain insight to this possibility, we simulated waveforms for a small set of events using SPiRaL and independent waveform-based models for comparison. For the events tested, the performance of the traveltimes-based SPiRaL model is shown to be generally on par with regional 3-D waveform-based models in three regions (western United States, Middle East, Korean Peninsula) suggesting SPiRaL may serve as a starting model for FWI over broad regions.

**Key words:** Composition and structure of the mantle; Body waves; Earthquake monitoring and test-ban treaty verification; Seismic anisotropy; Seismic tomography; Surface waves and free oscillations.

## 1 INTRODUCTION

Global seismic tomography continues to evolve and improve due to the constant increase in data availability and computational resources. Progress in this field of study has been well documented in reviews including Romanowicz (2003), Zhao (2015), Tromp (2019) and Ritsema & Lekic (2020) which describe the historic context and current advancements in detail. There are several examples of global-scale, whole-mantle tomography studies performed over the latter part of the last decade that consider a wide variety of data types

and improved methods, documenting the continued advancement in this research area (e.g. Zhao *et al.* 2013; Auer *et al.* 2014; Chang *et al.* 2015; French & Romanowicz 2015; Simmons *et al.* 2015; Tesoniero *et al.* 2015; Afanasiev *et al.* 2016; Ballard *et al.* 2016; Bozdag *et al.* 2016; Koelemeijer *et al.* 2016; Durand *et al.* 2017; Fichtner *et al.* 2018; Lu *et al.*, 2019, 2020; Hosseini *et al.* 2020; Lei *et al.* 2020; Toyokuni *et al.* 2020).

These recent studies represent several improvements including: multifrequency  $P$ -wave tomography (e.g. Hosseini *et al.* 2020), joint inversions of  $P$  and  $S$  body waves (e.g. Simmons *et al.* 2015;

Tesoniero *et al.* 2015; Koelemeijer *et al.* 2016; Lu *et al.* 2019), incorporation of complicated regional phases (e.g. Simmons *et al.* 2015), combined body and surface waves speeds with anisotropy (e.g. Auer *et al.* 2014; Chang *et al.* 2015; Tesoniero *et al.* 2015), joint seismic-geodynamic inversions (e.g. Lu *et al.* 2020), the addition of normal mode splitting functions (e.g. Koelemeijer *et al.* 2016; Durand *et al.* 2017), multiresolution models (e.g. Auer *et al.* 2014; Ballard *et al.* 2016; Toyokuni *et al.* 2020) and waveform inversions (e.g. French & Romanowicz 2015; Afansiev *et al.*, 2016; Bozdag *et al.* 2016; Fichtner *et al.* 2018; Lei *et al.* 2020). Each venture has some underlying purposes and goals that range from providing a basic understanding of the Earth's composition and evolutionary processes on global and/or regional scales to providing predictive capability for earthquake location, source characterization, or other applications.

Lawrence Livermore National Laboratory hosted a workshop in 2007 June in Berkeley, California that brought together academic, government and industry researchers to explore the potential for 3-D seismic models to contribute to applications of societal importance including seismic monitoring. The summary and conclusions resulting from this workshop were documented in Zucca *et al.* (2009). Following the guidance in Zucca *et al.* (2009), our objectives were to first construct global models that could accurately predict traveltimes at teleseismic and regional distances for improved event location (Simmons *et al.* 2011, 2012, 2015). Up to this point, our emphasis has been placed on the location of the events used in the inversions and the treatment of the shallow upper mantle (<200 km depth) needed to predict accurate regional traveltimes for monitoring smaller events (with limited teleseismic signal). The efforts were subsequently proven successful for reducing event mislocation errors when combining regional and teleseismic traveltime observations (Myers *et al.* 2015). The current study addresses the next phase to construct a global-scale model that predicts accurate traveltimes at all distances (for event location) as well as surface-wave dispersion for periods >20 s (for source characterization) with a single, self-consistent model of the Earth's crust and mantle (i.e. a common lithospheric model for each data type/application).

In this paper, we describe the development of a multiresolution ( $0.25^\circ$  to  $2^\circ$  node spacing) global model using millions of body wave traveltimes ( $P$  and  $S$  waves) and surface wave constraints (dispersion maps) for fundamental Rayleigh and Love waves at 25–200 s periods. The model, named SPiRaL ( $S = S$  waves,  $P = P$  waves,  $R = \text{Rayleigh waves}$ ,  $L = \text{Love waves}$ ), incorporates several elements from our previous model studies including: data set based on Bayesian multiple-event relocation, hierarchical tessellation model design, undulating surfaces and discontinuities, seven crustal units, 3-D ray tracing and multipathing, local and regional phases and a multiresolution inversion process. The major new elements in SPiRaL are the incorporation of surface wave constraints, additional body wave data, vertical transverse isotropy (VTI) media with five free parameters at each node throughout the crust and mantle and refined spherical tessellation grids with node spacing as small as  $\sim 0.25^\circ$  in some regions.

A longer term goal is to construct global seismic models capable of predicting accurate traveltimes (body waves and surface wave dispersion at long periods) and complete seismic waveforms with periods 10–50 s over broad regions and possibly the globe. One potentially viable path forward is to go directly to full-waveform inversion (FWI) without starting with a high-resolution global model similar to SPiRaL. A recent global FWI study by Lei *et al.* (2020) targeted periods as short as 17 s. Following the most common practice, Lei *et al.* (2020) began with a smooth starting model created using

**Table 1.** Body wave traveltime data.

Phase	Number of arrivals
P	3378 870
Pn	449 041
PcP	47 333
pP	53 872
pwP	35 496
Pg	108 026
Pb	43 673
S*	20 728
SS*	17 835
ScS*	2699
SKS*	5642
SKKS*	2605
sS*	1463
Total	4153 981

\*Waveform correlation picks provided by the University of Texas (Grand 2002; Lu & Grand 2016).

long-period waveform inversion then added constraints from shorter period data. However, we posit that higher resolution models like SPiRaL could provide a starting point for global or multiregional FWI, thereby reducing the inherent nonlinearity of FWI and reducing the number of iterations needed to achieve fits to the shorter period waves (<20 s). We provide more insight to this possibility by performing full-waveform simulations using SPiRaL for three key events in regions of interest including western North America, the Middle East and northeast Asia. The results are compared to data and other waveform predictions based on a selection of independent regional models that were at least partly constrained using waveform fitting methods.

## 2 DATA

### 2.1 Body wave traveltimes

In this study, we consider more than 4 million body wave arrival times for a variety of  $P$  and  $S$  waves including crustal, regional and teleseismic phases (Table 1). Much of the original arrival time 'pick' data ( $P$ -wave phases) were compiled from a variety of publicly available sources including the International Seismological Centre (ISC, <http://www.isc.ac.uk>), the National Earthquake Information Center, (NEIC, <http://earthquake.usgs.gov/regional/neic>) and regional bulletins. In addition, we considered data from seismic deployments including the USARRAY (Transportable Array, etc.), PASSCAL deployments (<http://www.iris.edu>), refraction surveys and Peaceful Nuclear Explosions (PNEs) performed by the United States and former Soviet Union. In total, we considered >4 million  $P$ -wave traveltimes from a selection of well-recorded events designed to provide global data coverage (see Supporting Information S1).

In addition to the traveltime pick data described above, we also included  $S$ -wave measurements derived from waveform modelling (see Grand 2002; Lu & Grand 2016). These  $S$ -wave measurements include teleseismic phases, multiples (e.g. SS), and core phases (ScS, SKS, etc.). The measurements were made by cross-correlation of reflectivity synthetic seismic waveforms to actual data. Although the measurement process was semiautomated, visual inspection of each waveform and timing shifts were made to assure that the phase onset time was matched. For some events, this was an iterative process involving adjustments to the assumed seismic source properties including source duration time lengths. This data set has served as a core data set for recent tomographic studies including the

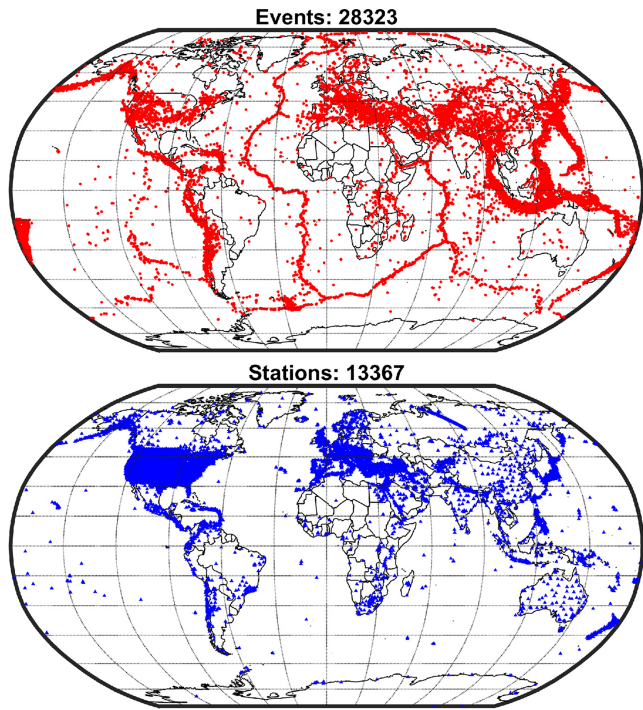


**Figure 1.** Seismic events and stations used in the body wave travelttime data set. Top: we selected 28 323 events distributed around the globe. See the text for our event selection strategy. Bottom: the 13 367 stations recording the >4 million body waves used in this study. Stations include numerous permanent and temporary deployments.

joint  $P$ - $S$  model produced in Simmons *et al.* (2015) and the joint seismic-geodynamic model produced more recently in Lu *et al.* (2020). Although this data set is small compared to the  $P$ -wave data set (~50 000 measurements), it provides important  $S$ -wave sensitivity and coverage not provided by the  $P$ -wave data including vertically travelling  $S$ -wave segments bouncing off Earth's solid surface. All together, we used 4153 981 travelttime arrivals from 28 323 events recorded at 13 367 stations distributed around the globe (Fig. 1). The body wave data coverage is highly variable given the available event and station configurations, especially in the crust and upper mantle (Figs S1–S3, Supporting Information). Similar to our previous studies (Simmons *et al.*, 2011, 2012, 2015), we applied the Bayesloc multiple-event location algorithm (Myers *et al.*, 2007, 2009, 2011) prior to inversion. The significance of the Bayesloc multiple-event relocation method for the development of travelttime data for tomography has been demonstrated in our previous studies (see Supporting Information S2 for more details).

## 2.2 Surface wave constraints

Rather than utilize individual surface wave velocity measurements, we chose to leverage surface wave velocity maps derived from millions of fundamental mode surface wave measurements (Ma *et al.* 2014; Ma & Masters 2014). Ma *et al.* (2014) developed and employed a cross-correlation clustering technique to measure the phase and group velocities for Rayleigh and Love waves at distinct periods ranging from 25 to 200 s. Using their compiled data and millions of measurements, they constructed maps of surface wave velocity while accounting for the effects of azimuthal anisotropy which could contaminate the isotropic velocity result. Ma *et al.* (2014) also adopted the regularization procedure in Ma & Masters (2014)

that aims to produce uniform model errors around the globe. Smoothness was increased in regions with less dense data coverage including the centre of vast oceans and the southern polar cap region. See Ma *et al.* (2014) for coverage, resolution and checkerboard tests.

For each specific surface wave type and period, Ma *et al.* (2014) constructed maps of velocity within 41 252 equal area blocks with dimensions of  $1^\circ$  by  $1^\circ$  at the equator. Similar to the work described in Pasyanos *et al.* (2014), we interpolated each map of isotropic surface wave velocities (azimuthal anisotropy effects removed) to a set of 40 962 nodes defined by a spherical tessellation grid with  $\sim 1^\circ$  node spacing. All together, we interpolated Love wave phase velocity maps at 10 discrete periods in the 33–133 s range, Love wave group velocity maps at 9 discrete periods in the 33–100 s range, Rayleigh phase velocity maps at 12 discrete periods in the 29–200 s range and Rayleigh group velocity maps at 14 discrete periods in the 25–133 s range (see Fig. S4, Supporting Information, for examples). In total, 45 maps of surface wave velocity at 40 962 points on the Earth were constructed, effectively providing  $45 \times 40 962 = 1843 290$  surface wave constraints used in our modelling (see Table 2 for a summary). These maps provide important constraints on the crust and upper mantle that is sampled non-uniformly by body waves, particularly beneath the oceans and continental margins. Although the maps are corrected for azimuthal anisotropy variations, radial anisotropy must be treated since both Love and Rayleigh waves are being considered simultaneously. Our approach for treating radial anisotropy variations is described in the following sections.

## 3 MODELLING METHODS

### 3.1 Starting model and parametrization

The LLNL-G3D-JPS model (Simmons *et al.* 2015) is a global 3-D model of isotropic compressional and shear wave speeds ( $V_p$  and  $V_s$ , respectively) and was constructed with a subset of the body wave travelttime data used in the current study. LLNL-G3D-JPS was selected as the starting velocity model for SPiRaL to avoid severe nonlinear issues that arise due to the model dependence of ray paths and surface wave sensitivity estimates. The overall LLNL-G3D-JPS model architecture was also adopted for the SPiRaL model. Briefly, the models are node-based using hierarchical spherical tessellation grids and consist of 59 aspherical surfaces from the surface to the core with (Fig. 2). The models directly incorporate all CRUST1.0 (Laske *et al.* 2013) units (water, ice, sediments and crystalline crustal layers), undulations in the transition zone (Lawrence & Shearer 2008), ellipticity at the surface based on the WGS84 ellipsoid and hydrostatic mantle stretching (Nakiboglu 1982; Alessandrin 1989). It is important to note that the velocities in the crust were allowed to vary from CRUST1.0 in the construction of LLNL-G3D-JPS, but the discontinuities and layer thicknesses were not allowed to change anywhere in the model. See Simmons *et al.* (2011, 2012, 2015) for more details on the model architecture and specific information on the construction of LLNL-G3D-JPS.

The base tessellation grid in the crust and upper mantle has nodes with  $\sim 1^\circ$  spacing and the lower mantle has nodes with  $\sim 2^\circ$  spacing. In order to capture more details in data-rich regions in the upper mantle, we chose to refine the node grids similar to other global tomography studies (e.g. Sambridge & Faletti 2003; Boschi *et al.* 2009; Bodin & Sambridge 2009; Auer *et al.* 2014; Ballard *et al.* 2016; Toyokuni *et al.* 2020). For large swaths of North America and

**Table 2.** Surface wave constrains from Love/Rayleigh phase/group maps (Ma *et al.* 2014; Ma & Masters 2014).

Wave type	Phase/Group	Periods (s)
Love	Phase	133, 100, 80, 67, 57, 50, 44, 40, 36, 33
Love	Group	100, 80, 67, 57, 50, 44, 40, 36, 33
Rayleigh	Phase	200, 133, 100, 80, 67, 50, 44, 40, 36, 33, 31, 29
Rayleigh	Group	133, 100, 80, 67, 57, 50, 44, 40, 36, 33, 31, 29, 27, 25

Note: Each map was projected to a spherical tessellation grid with a node spacing of  $\sim 1^\circ$  providing 40 962 point estimates each. The 45 maps provide 1843 290 surface wave constraints ( $45 \times 40\,962$ ) in total.

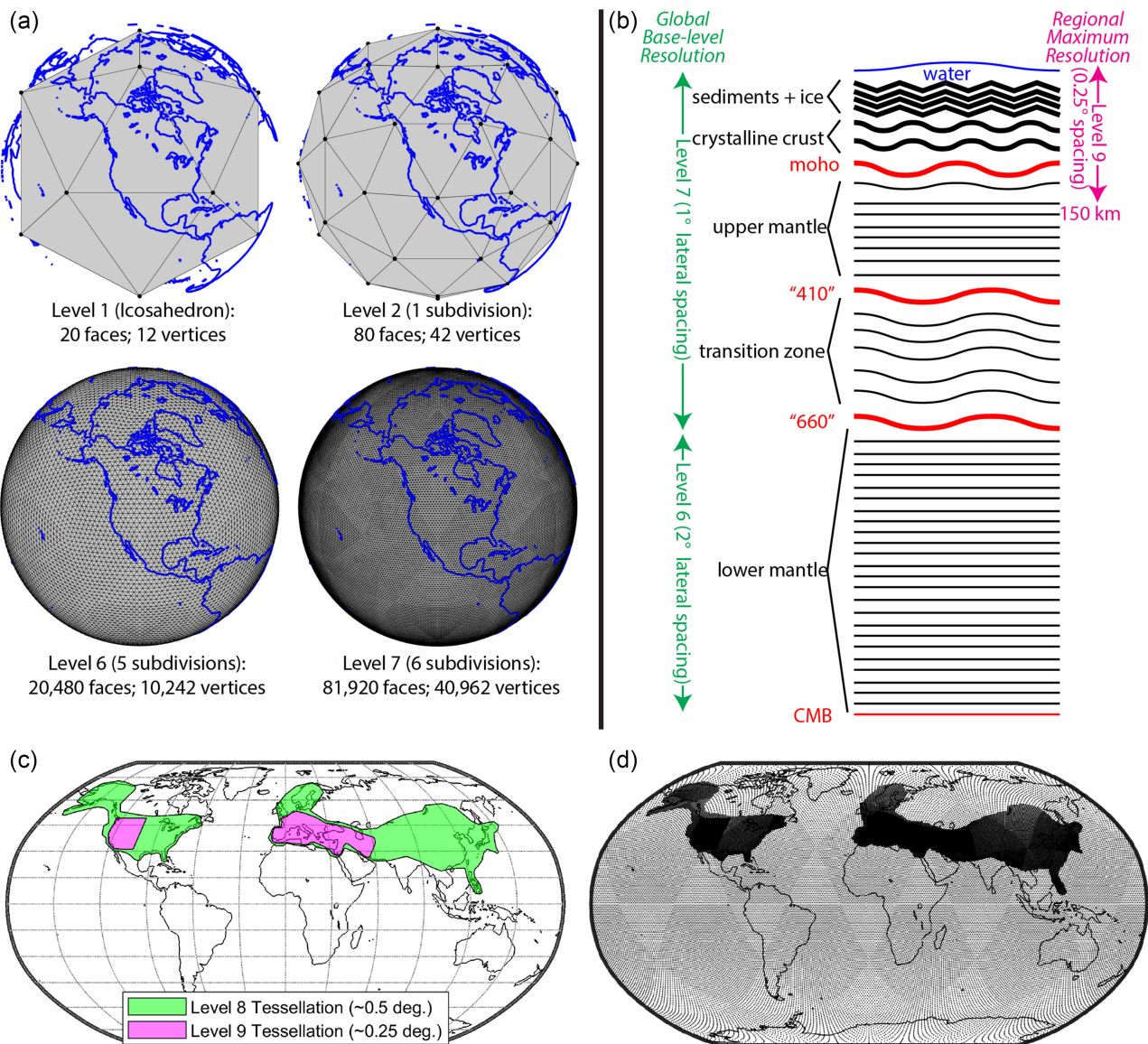


**Figure 2.** Model architecture and parametrization. (a) The lateral position of model nodes are defined by spherical tessellation grids developed through recursive subdivision of triangular faces. The ‘Level 1’ object represents an icosahedron, the ‘Level 2’ is the first subdivision of the icosahedron and so on. (b) The model consists of 59 crust and mantle surfaces with undulations and Earth’s asphericity (surface ellipticity and mantle stretching) built in. The base tessellation level for the crust and upper mantle is Level 7 ( $\sim 1^\circ$  node spacing) and Level 6 ( $\sim 2^\circ$  node spacing) in the lower mantle. (c) Regions with higher resolution grids than the base level. The crust and shallow upper mantle in the green and magenta regions are defined by the Level 8 and Level 9 tessellation grids ( $\sim 0.5^\circ$  and  $\sim 0.25^\circ$  grid spacing, respectively). (d) Node density in the shallow upper mantle.

Eurasia, the SPiRaL grid is refined to  $\sim 0.5^\circ$  nominal node spacing within the crust and shallow upper mantle down to 150 km. The grid is further refined down to  $\sim 0.25^\circ$  node spacing in subregions down to a depth of 115 km (see Fig. 2c). Velocities from the starting model were simply linearly interpolated to the refined nodes to complete

the construction of the SPiRaL starting model. The decision to refine the grids in these specific regions was based on a combination of data coverage (see Figs S1–S3, Supporting Information) and the resolution matrix calculations based on the LLNL-G3D-JPS model (Simmons *et al.* 2019). Altogether, the parametrization consists of

just over 2.1 million model nodes and starting compressional and shear velocities corresponding to the LLNL-G3D-JPS model.

The LLNL-G3D-JPS starting model was constructed solely with body waves and does not include terms for anisotropy. At a minimum, radial anisotropy (transverse isotropy with a vertical symmetry axis) must be considered with the addition of Love and Rayleigh waves to the SPiRaL model. Surface waves are dominantly sensitive to shear wave velocities which vary depending on the polarization. Specifically, Love waves are sensitive to horizontally polarized shear velocity ( $V_{sh}$ ) and Rayleigh waves are sensitive to vertically polarized shear velocity ( $V_{sv}$ ). If only considering laterally traveling surface waves and shear wave speeds, a single anisotropy term could be employed to describe the velocity difference for the two polarizations. However, SPiRaL includes  $P$  and  $S$  body waves that travel in all possible directions through the same media suggesting the need for additional anisotropy terms.

Radial anisotropy (or VTI) requires five terms in total to fully describe  $P$  and  $S$  wave velocities with horizontal and vertical polarizations for waves travelling in all directions. A common parametrization for radial anisotropy media involves the five Love parameters commonly known as  $A$ ,  $C$ ,  $L$ ,  $N$  and  $F$  (Love 1927). Alternatively, Thomsen (1986) formulated an intuitive set of linear equations that describe VTI media:

$$\begin{aligned} V_P(\theta) &= \alpha_0 (1 + \delta \sin^2 \theta \cos^2 \theta + \varepsilon \sin^4 \theta) \\ V_{SV}(\theta) &= \beta_0 \left[ 1 + \frac{\alpha_0^2}{\beta_0^2} (\varepsilon - \delta) \sin^2 \theta \cos^2 \theta \right] \\ V_{SH}(\theta) &= \beta_0 (1 + \gamma \sin^2 \theta) \end{aligned} \quad (1)$$

In eq. (1), the parameters include vertical  $P$ -wave speed ( $\alpha_0$ ), vertical  $S$ -wave speed ( $\beta_0$ ), three parameters controlling the anisotropy ( $\delta, \varepsilon, \gamma$ ) and the propagation direction angle relative to vertical ( $\theta$ ). The above relationships were shown by Thomsen (1986) to be valid for weak elastic anisotropy which is applicable to bulk Earth materials. For SPiRaL, we consider all five velocity parameters ( $\alpha_0, \beta_0, \delta, \varepsilon, \gamma$ ). For the starting model, the vertical wave speeds ( $\alpha_0, \beta_0$ ) were set to the velocities from LLNL-G3D-JPS and the anisotropy terms ( $\delta, \varepsilon, \gamma$ ) were set to zero.

### 3.2 Tomography

Seismic tomography involves the development of a system of equations that relate an Earth model to seismic observations and performing an inversion to update the current model to improve the misfit. In this work, the generalized system equations can be written in matrix form:

$$\begin{matrix} \text{S slowness derivatives} & \text{VTI param. derivatives} & \text{Data residuals} \\ \text{P slowness derivatives} & \text{Model} & \Delta t \\ \text{Travel times} & \frac{\partial t}{\partial U_S} & \Delta t \\ \text{Phase velocities} & \frac{\partial c}{\partial c} & \Delta c \\ \text{Group velocities} & \frac{\partial U_S}{\partial U_S} & \Delta U \\ \text{P/S slowness coupling} & \lambda_R f(R_{P/S}) & \Delta \delta \\ \text{Vertical S slowness damping} & -\lambda_R & 0 \\ \text{Vertical P slowness damping} & 0 & 0 \\ \text{VTI Parameter damping} & 0 & 0 \end{matrix} = \begin{matrix} \Delta t \\ \Delta c \\ \Delta U \\ \Delta \delta \\ \Delta \varepsilon \\ \Delta \gamma \end{matrix} \quad (2)$$

The parameters in eq. (2) are described in Table 3. The travel-time derivatives (ray path segment lengths) and data residuals were

**Table 3.** Variables in the matrix eq. (4).

Variable	Description
$t$	Body wave traveltimes
$C$	Surface wave phase velocities
$U$	Surface wave group velocities
$U_S$	Vertical shear wave slownesses
$U_P$	Vertical compressional wave slownesses
$\delta$	Thomsen VTI parameter <sup>†</sup>
$\varepsilon$	Thomsen VTI parameter <sup>†</sup>
$\gamma$	Thomsen VTI parameter <sup>†</sup>
$\lambda_R$	Vertical slowness coupling weight
$f(R_{P/S})$	Relative heterogeneity ratios converted for slowness perturbations <sup>‡</sup>
$\lambda_{U_S}$	Vertical shear slowness damping weight
$\lambda_{U_P}$	Vertical compressional slowness damping weight
$\lambda_\delta$	Thomsen VTI parameter damping weight
$\lambda_\varepsilon$	Thomsen VTI parameter damping weight
$\lambda_\gamma$	Thomsen VTI parameter damping weight

<sup>†</sup>Thomsen VTI parameters defined in Thomsen (1986).

<sup>‡</sup>Relative heterogeneity ratios from GyPSuM (Simmons et al. 2010).

determined via 3-D ray tracing through the model and taking the difference between the observed and predicted traveltimes ( $\Delta t$ ). The custom 3-D ray tracing method is adapted from Zhao et al. (1992) and considers multipathing (Simmons et al. 2011). While the 3-D ray tracing method uses the isotropic velocities to determine the ray paths, modifications were made to approximate the effects of the VTI media on the traveltimes (Supporting Information S3). Surface wave phase and group velocity derivatives (depth-dependent sensitivities) and data residuals were computed using a perturbation method applied at each surface node in the SPiRaL model using the *senskernel* software package provided by the University of Colorado Boulder (Supporting Information S4).

The system of equations in eq. (2) describes a generalized system and we employ the iterative LSQR algorithm (Paige & Saunders 1982) to solve such systems. More completely, we apply the *Progressive Multi-level Tessellation Inversion* (PMTI) technique (Simmons et al. 2011) which solves for the model variations at successively finer scales. The model is therefore refined through a series of inversions with increasing resolution as defined by the spherical tessellation grid recursions and model layer groupings. The PMTI method provides some intrinsic smoothing regularization, therefore only damping terms are used to control the model amplitudes. L-curve analysis was performed to determine the appropriate damping weights (Supporting Information S5; Fig. S5).

In addition to damping terms, eq. (2) includes  $P$ - and  $S$ -wave slowness coupling using the depth-dependent relative heterogeneity ratio profile ( $R_{P/S}$ ) from the joint seismic-geodynamic global tomography model (GyPSuM) developed in Simmons et al. (2010). Although the  $V_P$ - $V_S$  coupling term is included to guide the model, the perturbations of  $P$  and  $S$  wave speeds were not strictly enforced. The choice to relax this enforcement is based on the expectation of non-thermal (e.g. compositional) contributions to heterogeneity in the shallow upper mantle, leading to deviations from the temperature-based  $R_{P/S}$  scaling relationship. While most of the mantle heterogeneity can be explained by temperature variations alone (e.g. Schuberth et al. 2009), scaling factors need to diverge from a simple thermal expectation in the top  $\sim 250$  km of the mantle to simultaneously fit a suite of seismic and geodynamic constraints (Simmons et al. 2010).

Finally, the nonlinearity of the problem (sensitivity depends on structure) was addressed by performing three complete cycles of

multiresolution kernel calculation and model updating with PMTI, involving substantial computational resources (see Supporting Information S5 for details).

## 4 RESULTS

### 4.1 SPiRaL velocities

The compressional and shear velocities ( $V_p$  and  $V_s$ , respectively) for select depths in crust and mantle are shown in Figs 3–6 for the SPiRaL model. The velocities are expressed as bulk Voigt averages of horizontally and vertically polarized waves ( $V_{sh}$ ,  $V_{sv}$ ,  $V_{pv}$  and  $V_{ph}$ ) (e.g. Panning & Romanowicz 2006; Tesoniero *et al.* 2015). Beneath the continents, the pattern of wave speeds in the crust is similar overall to Crust1.0 (Laske *et al.* 2013). However, additional details and intensity differences are evident in the continental crust, most notably along the Tethyan margin extending from Europe to the Tibetan Plateau (Fig. 3). Overall, the most notable differences between SPiRaL and Crust1.0 occurs beneath the oceans where the SPiRaL model is consistently faster. The crustal velocity differences beneath the oceans is almost entirely driven by the surface waves since body wave constraints are severely limited, and it appears that both Love and Rayleigh waves force a faster crust beneath these regions. We are hesitant to develop any significant interpretation of these fast oceanic crust anomalies because of the trade-off of velocities and crustal thickness which is not allowed to vary in the modelling process.

In the shallow upper mantle (down to  $\sim$ 150 km depth), the SPiRaL mantle velocities beneath the continents tends to be fast while the mantle beneath the oceans tends to be slow (Fig. 4). This general result is expected based on previous tomography results that find relatively fast (cold) cratonic regions and slow (warm) zones near mid-ocean ridges. However, while the low  $V_s$  anomalies beneath tend to track the mid-ocean ridges, the low  $V_p$  anomalies tend to be dispersed and widespread in the shallow upper mantle beneath the oceans.

As mentioned previously in Section 3, we allowed for  $V_p$  and  $V_s$  patterns to diverge by relaxing the  $V_p$ – $V_s$  coupling enforcement in the inversion since we expect compositional and/or complex thermal effects that would not adhere to 1-D thermal scaling factors in the shallow upper mantle based on our previous work (Simmons *et al.* 2010). Indeed, the  $V_p$  and  $V_s$  patterns do diverge at these depths leading to interesting  $V_p$ – $V_s$  ratio patterns right below the Moho (Fig. 5). In the shallowest upper mantle, we find the average  $V_p$ – $V_s$  values of  $\sim$ 1.70 beneath the oceans with some locations below the Pacific Ocean dipping just below  $\sim$ 1.65. While these  $V_p$ – $V_s$  ratios are not usually seen in other global-scale models, similar ratios have been observed in several detailed surveys involving the shallowest part of the upper mantle (e.g. Zheng & Lay 2006; Mjelde *et al.* 2007; Kandilarov *et al.* 2015). Specifically, Zheng & Lay (2006) found  $V_p$ – $V_s$  values as low as 1.6 beneath the Sea of Okhotsk using underside reflections from deep sources. Perhaps more relevant to our findings beneath the oceans are results from ocean bottom seismometer (OBS) surveys near the Jan Mayen Ridge beneath the northern Atlantic Ocean (Mjelde *et al.* 2007; Kandilarov *et al.* 2015). In these detailed OBS deployment studies, the researchers found  $V_p$ – $V_s$  ratios as low as 1.65 in the shallowest upper mantle in the vicinity of the deployment. The authors point out that the values are consistent with un-serpentinized upper-mantle peridotite based on the work of Holbrook *et al.* (1992).  $V_p$ – $V_s$  ratios are commonly used as an indicator of serpentinization in the upper mantle and it

has been shown that the ratio increases in the vicinity of subduction zone trenches due to bending and faulting of the downgoing plate leading to infiltration of water and thus serpentinization (Grevermeyer *et al.* 2018). Although there may be a physical explanation for these  $V_p$ – $V_s$  ratio patterns, we note the high degree of uncertainty due to potential parameter trade-offs (velocity and anisotropy parameters) and overall sensitivity of Rayleigh waves to  $V_p$  which is small compared to sensitivity to  $V_s$ .

Further below the Moho (115 km depth) correlation between  $V_p$  and  $V_s$  anomalies is higher than in the shallower mantle beneath the oceans (Fig. 4). However, the lowest  $V_p$  anomalies beneath the Pacific Ocean are west of the East Pacific Ridge (EPR). This surprising result is similar to a previous study that combined surface and body waves (Tesoniero *et al.* 2015). In the Tesoniero *et al.* (2015) study, they developed a ‘preferred model’ (SPani) and a ‘test model’ called SPani\_test. In their test model,  $V_p$  and  $V_s$  were largely uncoupled so that the patterns of  $V_p$  and  $V_s$  could be quite different. Interestingly, they also found low  $V_p$  anomalies off axis from the EPR in the test (uncoupled) model which is similar to our result. Ultimately, the authors chose to more strictly enforce scaling between  $V_p$  and  $V_s$  perturbations leading to strongly matching patterns in their preferred model. We chose a different approach that allows for the wave speeds to diverge for the reasons stated above (expected strong divergence from simple scaling relationships in the shallow upper mantle). We believe that both approaches are valid and posit that the similarity of the SPani\_test and SPiRaL models (developed independently with different data, parametrizations and methods) may indicate that  $V_p$  in the shallow upper mantle beneath the oceans are lower than what is expected due to simple thermal effects. However, we recognize that the shallow upper mantle  $V_p$  beneath the oceans is almost entirely controlled by the Rayleigh wave maps (one data type with relatively low sensitivity to  $V_p$ ). and more research is needed to resolve this part of the mantle.

Notable features in the deeper upper mantle (below 150 km) includes the commonly observed low velocities along the East African Rift zone that extends down through the entire upper mantle. In addition, low  $V_p$  values are observed beneath many continental regions in the asthenosphere (Fig. 4, 265 km), most notably beneath southern and central Eurasia. The origin of these low  $P$ -wave speeds is unknown, but it is important to note that this is one of the more difficult parts of the mantle to resolve with our data. This difficulty is due to waning surface wave sensitivities near these depths and body wave ray paths do not tend to turn in this region due to low-velocity shadow zones. Regional body waves tend to turn either at depths shallower than 150 km or within the top of the transition zone, limiting sensitivity in the asthenosphere. Notable features in the transition zone include subducted slabs possibly deflected in the transition zone and/or stagnated along convergent margins throughout Eurasia. In addition, we detect a strong low-velocity anomaly in the transition zone beneath Hawaii.

In the lower mantle, the SPiRaL model has many features commonly seen in other models including the fast subducting slab anomalies along the ancient Farallon and Tethyan subduction zones beneath North America and Eurasia (Grand *et al.* 1997; van der Hilst *et al.* 1997). Also similar to all global tomography models, large low-velocity anomalies beneath the Pacific and African plates dominate the structures in the deepest mantle. We note that the patterns of  $V_p$  and  $V_s$  anomalies are very similar throughout most of the lower mantle indicating that  $P$ - and  $S$ -wave data are consistent with a simple thermal scaling relationship at these depths. However, the relative intensity of  $V_p$  and  $V_s$  anomalies varies in the deepest part of the large low velocity anomalies near the core–mantle

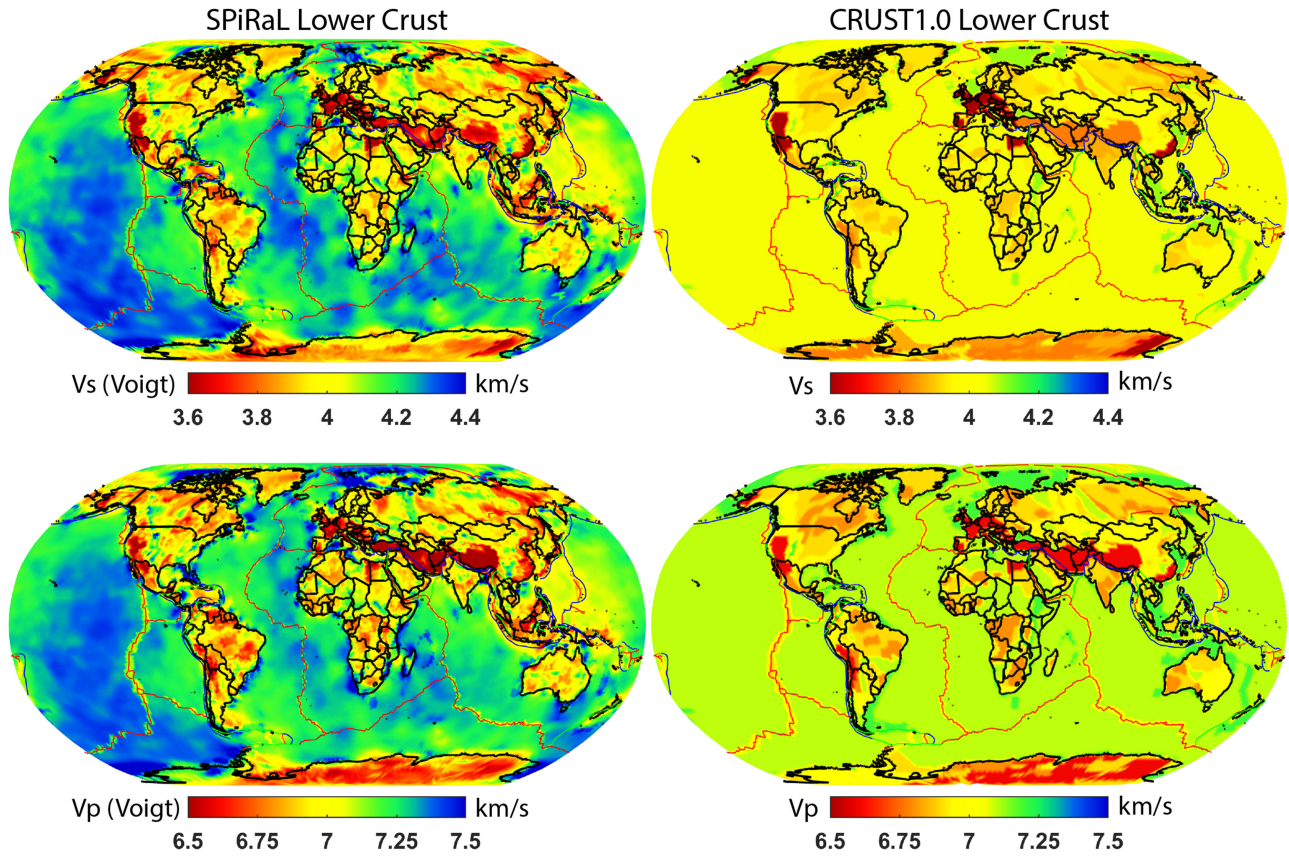


**Figure 3.** Shear and compressional velocities in the crystalline lower crust. Left-hand column: Voigt average  $V_s$  and  $V_p$  for the SPiRaL model. Right-hand column: isotropic  $V_s$  and  $V_p$  for the Crust1.0 model for comparison.

boundary (CMB). Multiple studies have shown these anomalies have non-thermal signatures including global-scale models using mode splitting data (e.g. Ishii & Tromp 1999) and joint seismic-geodynamic inversions (e.g. Simmons *et al.* 2007). Some of the differences between SPiRaL and a few other recent models are highlighted in the following sections.

#### 4.2 Anisotropy

As described in Section 3, the SPiRaL inversion includes terms to account for VTI variations expressed as five Thomsen parameters in eq. (1). Maps of anisotropy variations in SPiRaL are shown in Fig. 7 expressed as  $\xi = (V_{sh}/V_{sv})^2$  for shear waves and  $\varphi = (V_{pv}/V_{ph})^2$  for compressional waves. In the crust, anisotropy variations are strongest beneath the continents with both positive and negative depending on location, and shear wave anisotropy tends to be stronger than compressional anisotropy variations (throughout the mantle as well). We do not recognize any overall trend, but rather mostly scattered variations beneath the continents. However, positive  $\xi$  values are observed throughout much of the oceanic crust (i.e.  $V_{sh}$  is slightly faster than  $V_{sv}$ ).

In the shallow upper mantle (Moho to  $\sim 200$  km depth), the intensity of the anisotropy is strongest (Fig. 7). The shear wave anisotropy is stronger than compressional with  $\xi$  values exceeding 1.08 (i.e.  $V_{sh}$  faster than  $V_{sv}$  by more than about +4 per cent) in some areas. Although there is some scatter in the shallowest upper mantle, the primary result is that  $V_{sh}$  tends to be faster than  $V_{sv}$  almost everywhere around the globe down to  $\sim 200$  km depth which is largely consistent with other studies (e.g. Chang *et al.* 2015). The

compressional anisotropy in the shallow upper mantle is overall weaker and has more complex patterns. Near the Moho, we find modest consistent low  $\varphi$  values ( $V_{pv} < V_{ph}$ ) beneath the oceans and modest high  $\varphi$  values ( $V_{pv} > V_{ph}$ ) beneath the continents. The pattern of  $\varphi$  shifts at  $\sim 150$  km depth where we find  $\varphi > 1$  beneath most regions with the exception at the EPR which shows  $\varphi$  slightly less than 1 ( $V_{pv} < V_{ph}$ ) which is likely related to the strong lateral flow beneath the fastest spreading ridge.

At depths  $> 200$  km, the intensity of the shear wave anisotropy drops dramatically with  $\xi$  values approaching the value of 1 ( $V_{sh} = V_{sv}$ ). The compressional anisotropy signatures are also relatively small at these depths, but we point out a consistent trend of low  $\varphi$  values beneath the oceans ( $V_{pv} < V_{ph}$ ). However, we urge caution in interpreting the compressional anisotropy results at these depths based on the limited sensitivity. Moreover, as pointed out in Tesoniero *et al.* (2015), the constraints on  $\varphi$  (measure of compressional anisotropy) are weak overall relative to bulk velocities and  $\xi$  (measure of shear anisotropy). In the current study, we do incorporate regional  $P$  waves that travel at various angles through the shallowest upper mantle beneath the continents, providing more constraints than teleseismic  $P$  waves that travel with almost vertical paths through most of the upper mantle. Nonetheless, we urge caution in interpreting  $\varphi$  in a geological sense.

Unlike  $\varphi$ , there are several independent models of  $\xi$  to compare to the SPiRaL model (Fig. 8). In Fig. 8, the mean (or 1-D) values of  $\xi$  are shown as a function of depth for SPiRaL and several previous models (Dziewonski & Anderson 1981; Montagner & Anderson 1989; Visser *et al.* 2008; Panning *et al.* 2010; French *et al.* 2013; Moulik & Ekström 2014; Chang *et al.* 2015; Tesoniero *et al.* 2015).

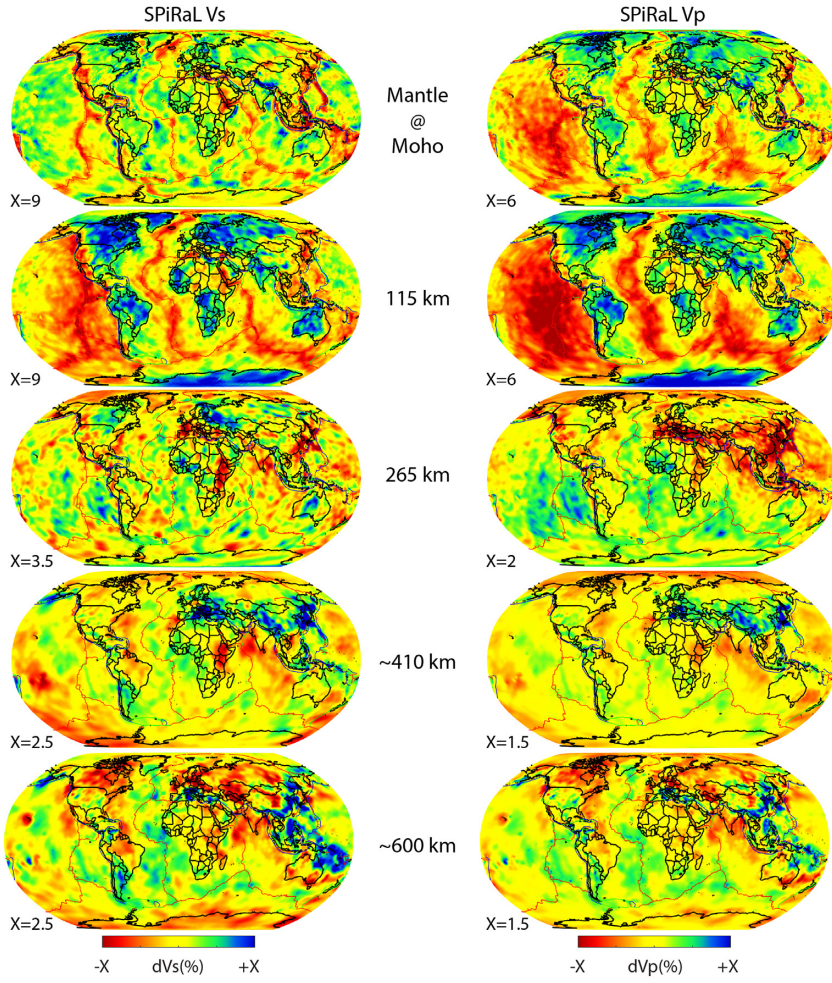


**Figure 4.** Upper-mantle shear and compressional wave velocities in the SPiRaL model shown as percentage variations relative to the global mean model.

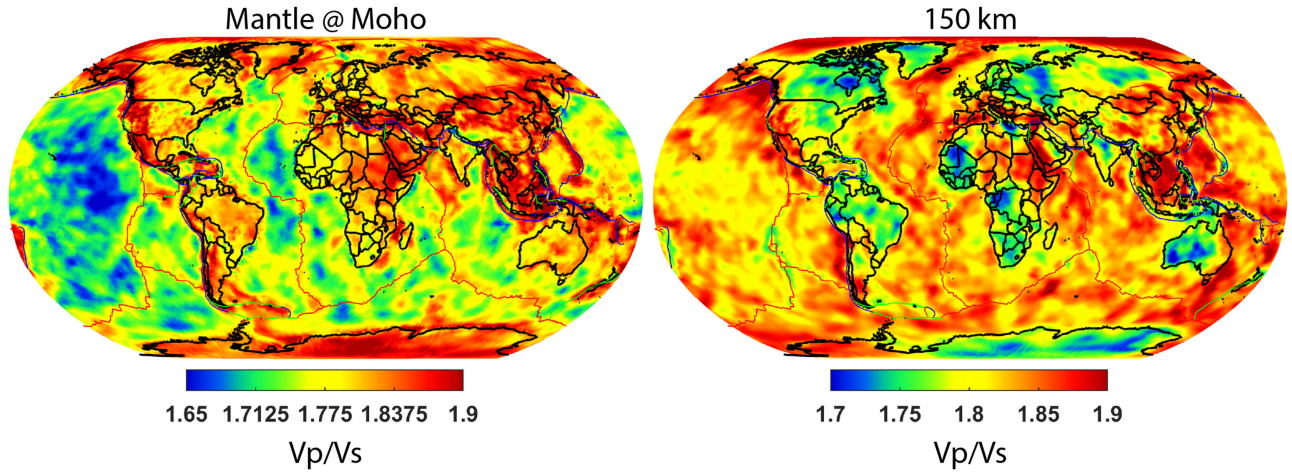


**Figure 5.** Shallow upper mantle  $V_p:V_s$  ratios in the SPiRaL model.

All shear anisotropy profiles show  $\xi > 1$  ( $V_{sh} > V_{sv}$ ) in the shallow upper mantle, often peaking in the 100–200 km depth range consistent with the average values in the SPiRaL model. The curves drop off drastically below  $\sim 220$  km depth, often with  $\xi < 1$  from 220–400 km depth (SPiRaL included). In the transition zone and deeper ( $> 400$  km), most all models show values very close to  $\xi = 1$ . Although there is significant 3-D variability of  $\xi$  in SPiRaL (see

shaded region in Fig. 8), we conclude that the mean values are highly consistent with past results overall.

#### 4.3 Data fits

Data fits for the SPiRaL model are shown for body waves (Fig. 9) and surface waves (Fig. 10). Overall, the body wave traveltimes are

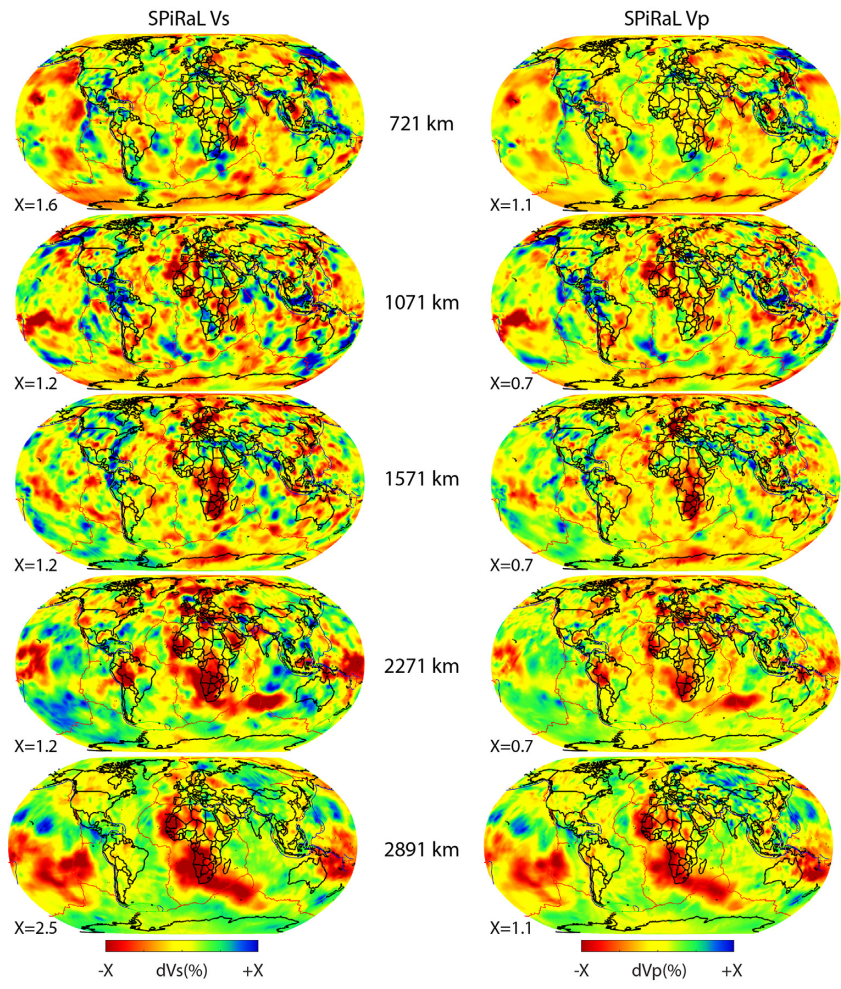


**Figure 6.** Lower mantle shear and compressional wave velocities in the SPiRaL model shown as percentage variations relative to the global mean model.

better fit than with the starting model (LLNL-G3D-JPS). The most notable improvements are with the  $S$ -wave phases and  $Pg$ . However, we note that relative improvement of the  $S$ -wave phases (on a percentage basis) are not substantially different than with the  $P$ -wave phases overall. The overall modest improvement is expected given the increased number of free parameters in the inversion, but there are some caveats to the general observation. First, we note that the  $Pg$  phases appear to be fit substantially better with SPiRaL. However, this metric is biased since the new  $Pg$  data set includes thousands of additional measurements for these arrivals at shorter distances overall (within  $\sim 1.2^\circ$ ) which tend to have smaller travel-time errors relative to arrivals at distances similar to  $4^\circ$  for example. We also note that two  $P$ -wave phases ( $pP$  and  $PcP$ ) are fit slightly less well with SPiRaL. We attribute these slight misfit increases to the addition of new data changing the relative weighting of the new systems of equations and data inconsistencies/disagreements that arise when new constraints are introduced to the inversion.

The largest improvements are the fits to the surface wave group and phase velocity (Fig. 10). Misfits for the surface waves are determined by comparing the predicted velocity for each phase type (Rayleigh or Love, phase or group) and period and calculating the root-mean-squared (RMS) difference from the surface wave maps constructed in Ma *et al.* (2014). We compare the SPiRaL surface wave fits to the starting model (LLNL-G3D-JPS) which was constructed with body waves alone, and the LITHO1.0 model

(Paschos *et al.* 2014) which was constructed using the same surface-wave data as SPiRaL. Note that the LLNL-G3D-JPS and LITHO1.0 models started with the CRUST1.0 model and the crust was modified in each inversion process. The crust is further modified from the LLNL-G3D-JPS model in the SPiRaL tomographic inversion. Not surprisingly, the LLNL-G3D-JPS model fits the surface wave data most poorly relative to the other models, and the SPiRaL model fits substantially better than the starting model. SPiRaL also fits the surface wave constraints better than the LITHO1.0 model. This result is also not surprising since the LITHO1.0 model had far fewer model parameters and did not include anisotropy. The main point regarding data fits is that SPiRaL fits surface waves well while also fitting a large set of body wave traveltimes simultaneously.

As described in Section 3, SPiRaL is built on a refined spherical tessellation grid with embedded high-resolution zones in the crust and shallow upper mantle throughout North America and Eurasia (Fig. 2). A direct comparison between the LLNL-G3D-JPS starting model ( $\sim 1^\circ$  minimum node spacing) and the new SPiRaL model with refined grids (node spacing as low as  $0.25^\circ$ ) is shown in Fig. 11 for  $Vp$  in the shallowest upper mantle beneath the western United States. The SPiRaL model shows more details and tends to have increased anomaly intensities relative to LLNL-G3D-JPS. However, we note newly imaged low-velocity trends in the SPiRaL model, including a across Wyoming from the Yellowstone volcanic area in northwest Wyoming to the southeast of the state and another low

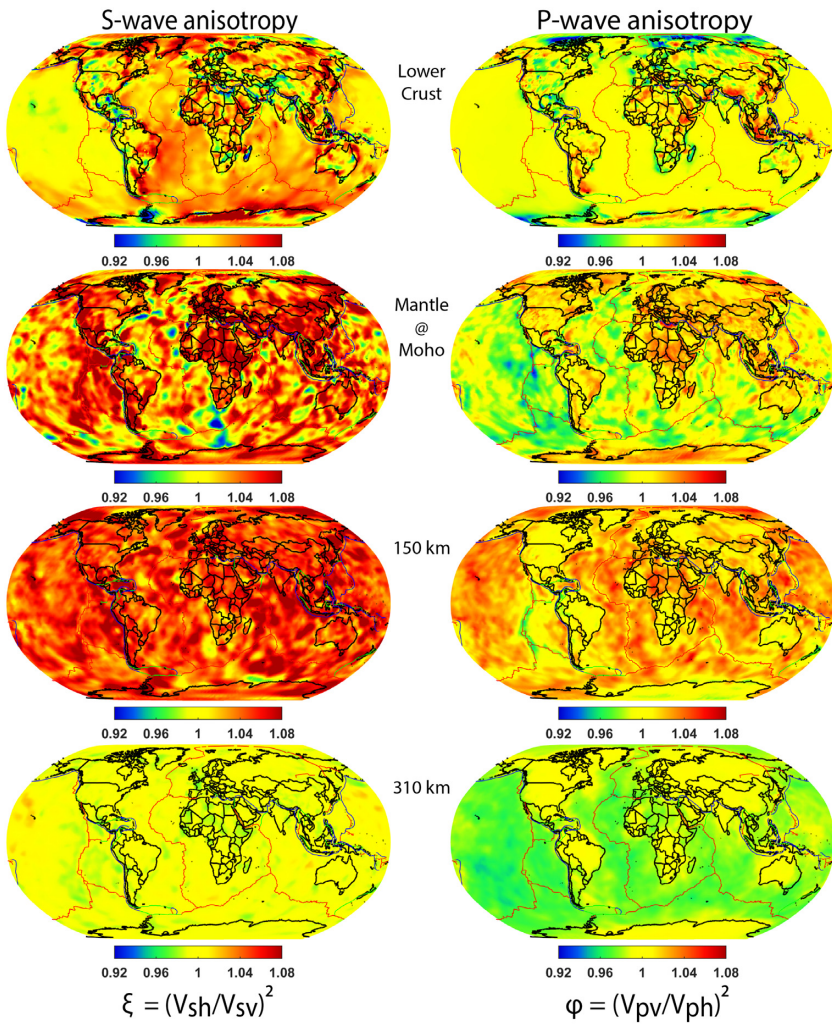


**Figure 7.** Transverse anisotropy variations in the SPiRaL crust and upper mantle. Left-hand column: shear anisotropy variations expressed as  $\xi = (V_{sh}/V_{sv})^2$ . Right-hand column: compressional anisotropy variations expressed as  $\varphi = (V_{pv}/V_{ph})^2$ . Note that all colour scales are the same to highlight the relative strength of anisotropy with depth.

velocity trend in central and northern California. Other than these two features, the overall broad-scale patterns of the two models are similar, but with more details emerging in SPiRaL. In regards to data fit, the additional nodes in the high-resolution regions have no significant impact on the fit to the surface wave velocity maps that are sampled on a  $\sim 1^\circ$  tessellation grid. The primary impact of these high-resolution zones is improved fit to regional and crustal  $P$ -wave body phases ( $Pn$ ,  $Pg$  and  $Pb$ ) that travel through these regions (Fig. S6). Relative to a  $2^\circ$  resolution model, the residual travelttime variance is reduced by  $\sim 19$  per cent for  $Pn$  and  $Pg$ , and  $\sim 12$  per cent for  $Pb$  when refining the grid to  $0.25^\circ$  node spacing.

#### 4.4 Global model comparisons

The SPiRaL global model and others are shown in Figs 12 and 13. We selected three other models to compare to including the starting model LLNL-G3D-JPS (Simmons *et al.* 2015), SPani (Tesoniero *et al.* 2015) and TX2019slab (Lu *et al.* 2019). The models were selected since they are all recent global-scale joint models of  $V_p$  and  $V_s$ . LLNL-G3D-JPS and TX2019slab were constructed with  $S$  and  $P$  body waves only and neither accounted for anisotropy, while the SPani model used  $S$  and  $P$  body waves, surface waves (fundamental

and higher modes) and also considered radial anisotropy. The SPani model is most similar to SPiRaL in terms of the data types used and properties determined; however, SPani was constructed using crustal corrections based on  $5^\circ \times 5^\circ$  block parametrization rather than directly incorporating a high-resolution crust into the model.

In the shallowest upper mantle, SPiRaL shows more broadened low-velocity anomalies beneath the mid-ocean ridges relative to the LLNL-G3D-JPS (starting) model. It should be noted that the LLNL-G3D-JPS mid-ocean ridge anomalies are only slightly different than the thermal starting model of the oceanic mantle which is part of the Crust 1.0 model. The SPani and TX2019 show similar broadened patterns in the shallowest upper mantle beneath the oceans, however SPiRaL anomalies are more intense and detailed overall. As previously discussed, some departure in patterns of  $V_p$  beneath the oceans is noticed as the low velocities beneath the East Pacific Rise are skewed westward of the ridge axis (Fig. 13). Tesoneiro *et al.* (2015) demonstrated that, when the scaling between  $V_p$  and  $V_s$  anomalies are loosely enforced, the SPani ‘test model’ yielded a similar result. We chose to relax thermal  $V_p$ – $V_s$  scaling based on evidence for significant compositional influence on velocity heterogeneity in shallow upper mantle. See Section 4.1 above for more discussion on this topic. Similar to the shallow upper mantle beneath

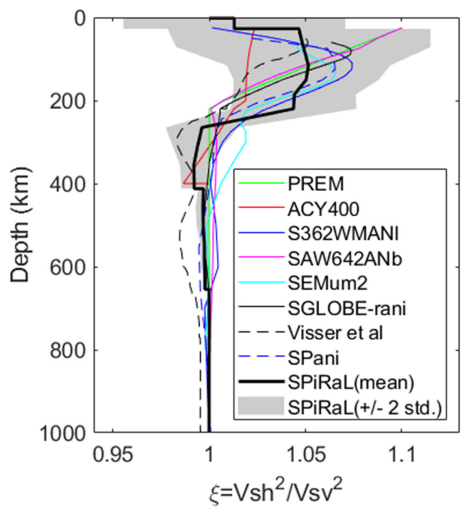


**Figure 8.** Vertical profiles of  $\xi = (V_{sh}/V_{sv})^2$  for several models including SPIRaL. The average values for SPIRaL is plotted as the heavy black solid line and the modelled range of values is shown in the grey shaded regions ( $\pm 2$  standard deviations about the mean). Models: PREM (Dziewonski & Anderson 1981), ACY400 (Montagner & Anderson 1989), S362WMANI (Moulik & Ekström 2014), SAW642ANb (Panning et al. 2010), SEMum2 (French et al. 2013), SGLOBE-rani (Chang et al. 2015), Visser et al (Visser et al. 2008) and SPani (Tesoniero et al. 2015).

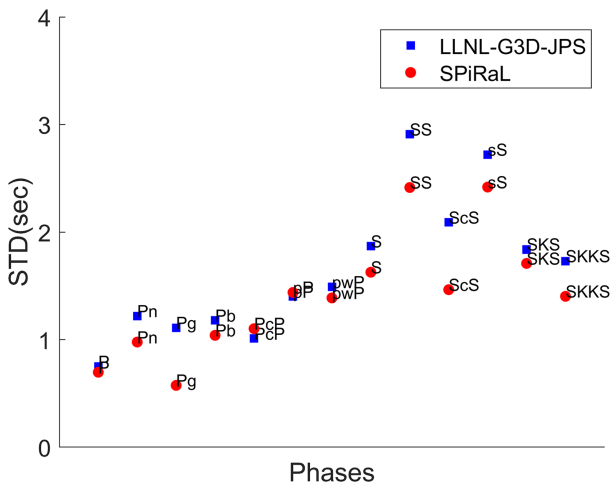


**Figure 9.** Body wave traveltimes for each phase considered. The fits for the SPIRaL model are compared to those starting model (LLNL-G3D-JPS, Simmons et al. 2015) which was constructed with body waves alone and without considering anisotropy.

the oceans, the fast regions beneath the continents are significantly more intense in the SPIRaL model compared to the other models shown here.

Significant variability in patterns and intensities is evident in the transition zone across the selected models. However, all models show some degree of broad fast anomalies in the transition zone along the western side of the Americas and along the western Pacific margin in East Asia. The SPIRaL and LLNL-G3D-JPS models differ from the other models along much of the Tethyan margin where they show broad and intense fast anomalies in the transition zone across Eurasia. We believe these differences are due to several factors including the use of many  $P$ -wave arrivals at regional distances as well as transitional distances where thousands of  $P$ -wave rays turn within the transition zone. While 3-D ray tracing could

also explain differences from some models of the upper mantle, we note that the TX2019 model (Lu et al. 2019) employed the same 3-D ray tracer and each model was developed with some data in common. However, there are several key differences including Bayesloc multiple-event relocation (used here), starting models (LLNL-G3D-JPS in this study versus a synthetic slab model) and parametrizations ( $1^\circ$  nodes in this study versus  $275 \times 275$  km blocks). In addition, the inversion technique is likely a significant contributor to the differences between TX2019 and SPIRaL since we used the PMTI multiresolution inversion without a smoothing operator and three iterations of inversion and ray tracing to account for nonlinearity (3-D ray paths and surface wave sensitivities depend on the model).

In the lower mantle, the differences between SPIRaL and the LLNL-G3D-JPS starting model are small. Also, many of the same features are observed across all models including the fast wave speed associated with subducted slabs along the ancient Farallon margin beneath the Americas as well as the ancient Tethyan margin across southern Eurasia ( $\sim 1200$  km depth). However, the intensity of these fast anomalies decrease at depths around 1800 km in SPIRaL and LLNL-G3D-JPS. In the deepest mantle, patterns become considerably more similar across all models which all show the dominant low-velocity anomalies beneath Africa and the central Pacific Ocean. These low-velocity features tend to be more intense in the SPIRaL and LLNL-G3D-JPS models relative to the other models considered (Figs 12 and 13). Likewise, the fast anomalies in the deepest mantle are also more intense in the SPIRaL and starting model relative to other models. These deep fast anomalies are presumably ancient subducted slab remnants resting atop the CMB, but it is not within the scope of this work to further argue this point.

## 5 WAVEFORM SIMULATIONS

This section explores the potential for using the high-resolution global SPIRaL model to serve as a starting model for FWI in multiple broad regions. There are several past and ongoing efforts across the broad community to construct global-scale FWI-based models (e.g. French & Romanowicz 2015; Afansiev et al., 2016; Bozdag et al. 2016; Fichtner et al. 2018; Lei et al. 2020). For monitoring applications and furthering imaging of Earth's interior, a single model that can predict waveforms with 10–50 s periods (either globally or over multiple broad regions) while simultaneously predicting accurate regional/teleseismic body wave traveltimes is ideal. We posit that the development of such a global Earth model might be more readily achievable by starting with a high-resolution traveltime-based model like SPIRaL. To gain insight into this possibility, we simulated full waveforms from a few key events in different regions using SPIRaL, the AK135 1-D model (Kennett et al. 1995), and independently developed regional 3-D models that were informed by waveforms in their construction. The key events we chose to simulate are listed in Table 4. These events include: (1) the 2008 Wells, Nevada earthquake; (2) the 2005 Qeshm, Iran earthquake and (3) the 6th declared nuclear test performed by the Democratic People's Republic of Korea (DPRK) that occurred on 2017 September 3. We chose these events because they occur in regions of interest for monitoring, are in different tectonic settings, and all regions have independently developed, waveform-informed regional 3-D tomography models to benchmark against.

We simulated waveforms to all available stations within a  $30^\circ$  arc distance using SPECFEM3D\_Globe (Komatitsch & Tromp 2002a, 2002b; Komatitsch et al. 2015) down to 10 s periods. To make a

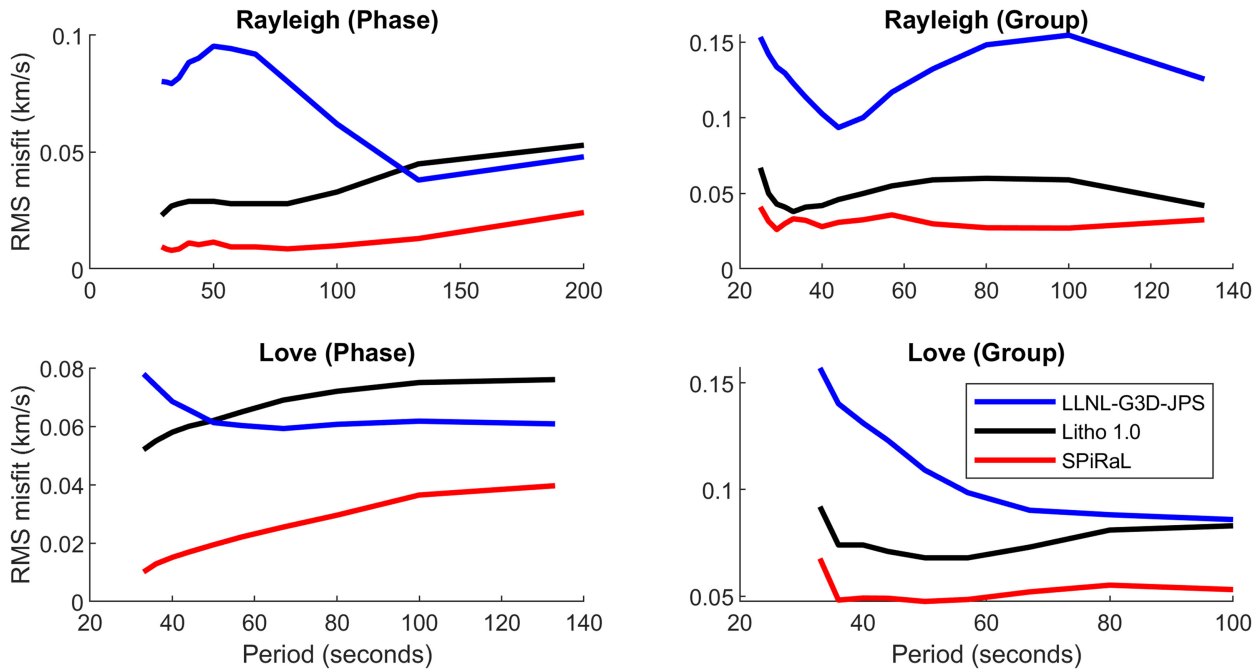


**Figure 10.** Surface wave misfits as a function of period for SPiRaL, the LLNL-G3D-JPS starting model and the LITHO1.0 model (Pasyanos *et al.* 2014).

quantitative comparison between models and simulations, we employed the Pyflex algorithms (Krischer & Casarotti 2015). Pyflex is a Python-based adaptation of the original FLEXWIN algorithm (Maggi *et al.* 2009) for automatically picking waveform time windows for seismic tomography applications. One application of the Pyflex utility is finding time windows within seismograms where phase time-shifts and amplitude differences between the data and synthetics can be used for FWI. There are several input parameters (11 in total) to Pyflex that are designed to find time windows within which observed and simulated waveforms show relatively good agreement. Parameters include maximum allowable phase time-shifts ( $Tshift$ ), minimum allowable cross correlation coefficients (CC) and maximum allowable amplitude differences ( $dlnA$ , where  $A$  is displacement). For each event, window picking parameters were tuned by evaluating how well the choice of parameters correctly identified phase shifts based on visual inspection of subsets of picked windows across many stations and channels. We then compiled the key statistics including CC,  $Tshift$ , and  $dlnA$  distributions. We also tracked the number of useable windows ( $Nwin$ ) and number of seismogram traces ( $Ntrace$ ) for each model to compare the number of seismograms and windows with acceptable misfit measurements to carry out FWI. This process was applied to two distinct period bands (20–50 and 10–20 s) and statistics for each band were compiled. Although the Pyflex input parameters were tuned for each event, we limited the maximum  $Tshift$  to one-half wavelength of the minimum period in the band. The results of this analysis are discussed in the following sections.

### 5.1 Results for the 2008 $M_w = 5.9$ wells, Nevada earthquake

The 2008 Wells, Nevada earthquake ( $M_w = 5.9$ ) was well recorded at regional and local distances on a large number of stations throughout the western US including the USArray TA. In total, we simulated waveforms to 296 stations in the region using SPiRaL, AK135 and

the SEMumNA14 upper-mantle model (Yuan *et al.* 2014) combined with US2016 model of the crust (Shen & Ritzwoller 2016). SEMumNA14 is a shear model of the upper mantle beneath North America with radial anisotropy constructed via waveform inversion using a spectral element method (RegSEM, Cupillard *et al.* 2012) and non-linear asymptotic coupling theory (Li & Romanowicz 1996). The model was based on waveform data provided by the USArray TA deployment. US2016 is an independent 3-D shear velocity model of the upper 150 km of the mantle beneath the United States based on surface wave dispersion from ambient noise and earthquakes, and additional data including receiver functions. To account for the crust missing from SEMumNA14 model, we chose to use the crustal portion of the US2016 model to form a ‘hybrid’ model (US2016+SEMumNA14). This choice was made based on a study that concluded this combination of models (US2016 in the crust and SEMumNA14 in the mantle) was a good starting model for FWI in the region (Zhou *et al.* 2021).

Waveforms for the Wells event are shown in Fig. 14 for station ARV in the Southern California Seismic Network at a distance of 753 km and Fig. S7 in the Supporting Information for TA station A16A at a distance of 905 km to the north. These waveforms demonstrate the variability of fit across the models, components and various time windows. Visual inspection of the seismograms gives us a qualitative sense that AK135 performs surprisingly well for this event. SPiRaL performs perhaps slightly better than the US2016+SEMumNA14 hybrid model, however there is some subjectivity. In the 20–50 s period band, more usable windows are found with the SPiRaL model than the other two models (223 for SPiRaL and 198 for each of the other models, see Fig. 15). Thus, SPiRaL predicts waveforms slightly better in this period band and would initially provide more misfit measurements which are key for model updating through adjoint FWI. However, we note that the distribution of amplitudes and time-shifts for the useable windows for the US2016+SEMumNA14 model tend to be more centred about zero. In the 10–20 s period band, the patterns of the

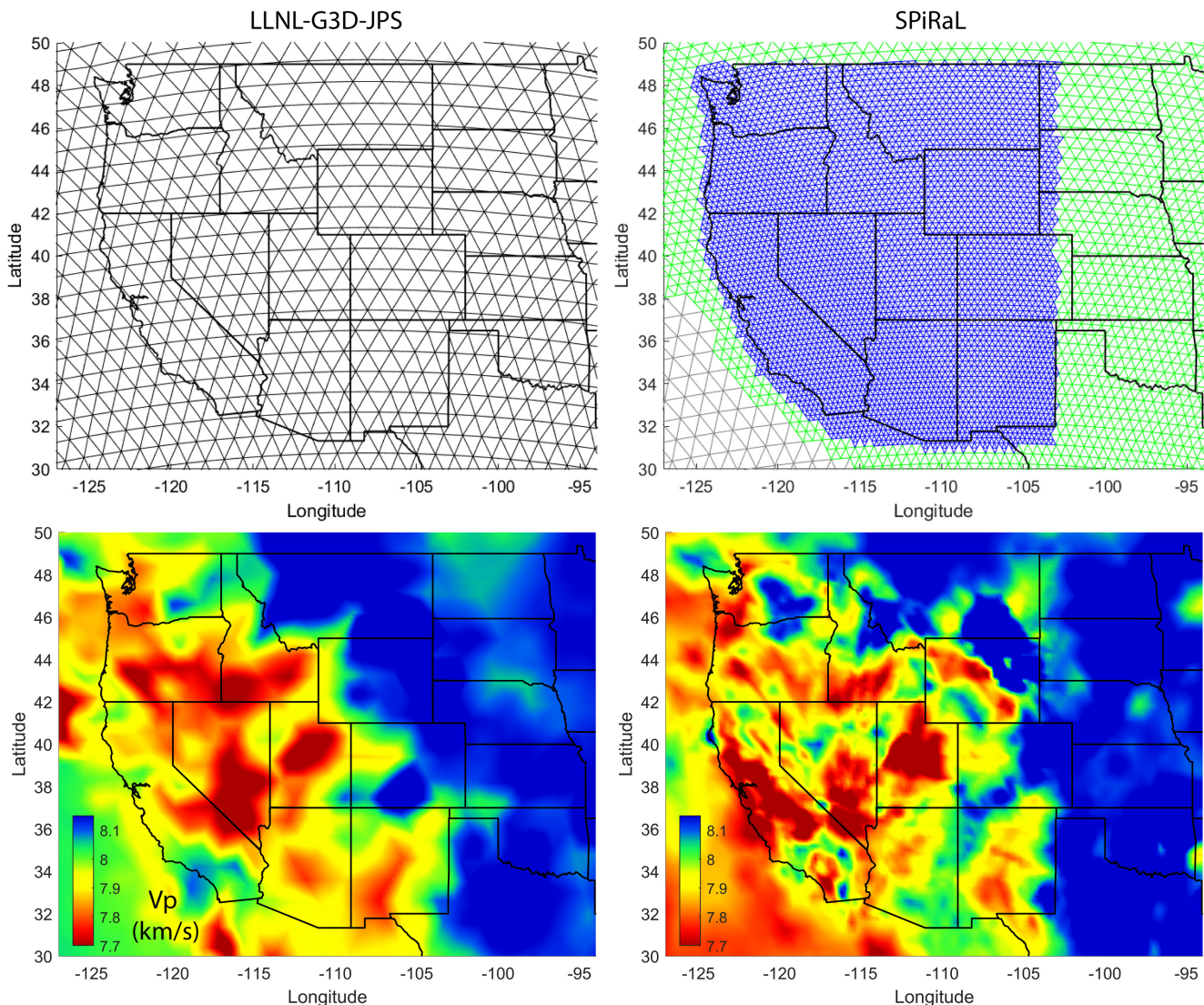


**Figure 11.** Comparison of LLNL-G3D-JPS and SPiRaL  $P$ -wave speeds in the shallowest upper mantle. Left-hand column: the spherical tessellation grid ( $\sim 1^\circ$  node spacing) used to parametrize the LLNL-G3D-JPS starting model (top) and the resulting image of  $V_p$  in the shallowest upper mantle (bottom). Right-hand column: the refined spherical tessellation grid (green =  $0.5^\circ$  node spacing and blue =  $0.25^\circ$  node spacing) used to construct the SPiRaL model (top) and the resulting high-resolution image of  $V_p$  (bottom). Note that the velocity scales have been adjusted for the overall slow upper mantle beneath the western United States.

waveform window fit metrics (cross correlation, time-shift and amplitude differences) are comparable, however SPiRaL yields many more useable windows than the other 3-D model (Fig. 16). Interestingly, the AK135 and SPiRaL models both yield a similar number of picked windows ( $N_{win} > 600$ ,  $N_{trace} \approx 500$ ) whereas the US2016+SEMumNA14 yielded far fewer time windows ( $N_{win} = 415$ ,  $N_{trace} = 351$ ). These findings confirm that AK135 predicts the waveforms quite well and SPiRaL is at least on par with the other 3-D model for this particular event.

## 5.2 Results for the 2005 $M_w = 6.1$ Qeshm Island, Iran earthquake

The 2005 Qeshm, Iran earthquake ( $M_w = 6.1$ ) was a destructive event beneath Qeshm Island in the Persian Gulf. Unlike the Wells earthquake, publicly available data are limited at near-regional distances ( $< 1200$  km). However, there are several recordings at

networks at further distances along multiple azimuthal corridors. These include recordings at stations comprising GEOFON, GeoScope and the Global Seismic Networks. In addition, data sources include the Dhofar Seismic Experiment, temporary IRIS Passcal deployments in Kyrgyzstan (Tien Shan) and Turkey (North Anatolian Fault Zone), the Boina Broadband Network in Ethiopia, National networks (e.g. Isreal, Kazakhstan, Tajikistan) and others. In total, we simulated and analysed waveforms to 154 stations using SPiRaL, AK135 and the S2.9EA model (Kustowski *et al.* 2008). The S2.9EA model is a global-scale model, but with emphasis on Eurasia where they used a higher resolution refined grid (spacing down to  $\sim 2.9^\circ$ ). The model was constructed with long-period surface wave waveforms, surface wave phase velocities and body wave traveltimes.

Example waveforms for the 2005 Qeshm Island event are shown in Fig. 17 for station ABKT in Turkmenistan at a distance of 1270 km and Fig. S8 in the Supporting Information for station ANTO in

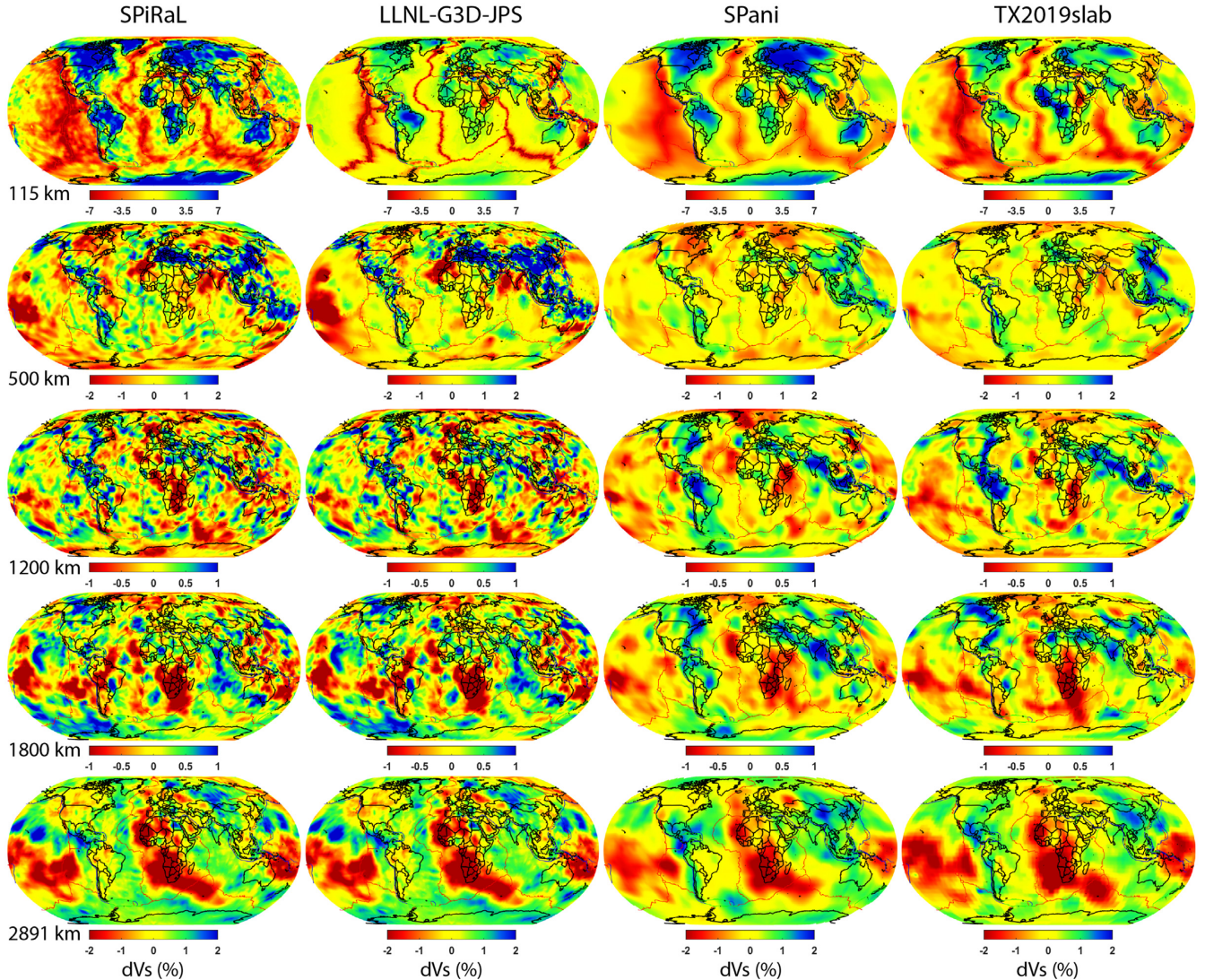


**Figure 12.** Comparison of SPiRaL  $V_s$  anomalies to other selected joint  $V_p$ - $V_s$  models. LLNL-G3D-JPS (Simmons *et al.* 2015), SPani (Tesoniero *et al.* 2015) and TX2019slab (Lu *et al.* 2019).

Turkey at a distance of 2587 km. Our overall qualitative (visual) assessment of the 20–50 s waveforms is that SPiRaL clearly predicts waveforms better than AK135 and is at least on par with S2.9EA for this event. The Pyflex window picking analysis is largely consistent with this assessment (Fig. 18). The largest number of windows is selected by Pyflex when using the SPiRaL model than with the other two models ( $N_{win} = 584$ ,  $N_{traces} = 354$ ), suggesting that using SPiRaL as a starting model would potentially result in more useable data (adjoint sources) for FWI. S2.9EA performs second best in terms of the number of selected windows ( $N_{win} = 485$ ,  $N_{traces} = 293$ ). However, we note that the  $T_{shift}$  distributions for SPiRaL are biased toward negative numbers whereas S2.9EA tend to be more centred about zero. It is possible that this time-shift could be rectified by adjusting the event origin time from the catalogue origin time which was not done here. SPiRaL arguably performs better than S2.9EA at matching amplitudes within the picked windows based on the distributions (Fig. 18). Our qualitative (visual) assessment of the 10–20 s waveforms for the Qeshm event suggests that SPiRaL performs better than AK135, but slightly underperforms S2.9EA within this period band. The Pyflex analysis supports this general

conclusion (Fig. 19). More waveform windows are selected with S2.9EA ( $N_{win} = 455$ ,  $N_{traces} = 305$ ) than with SPiRaL ( $N_{win} = 384$ ,  $N_{traces} = 291$ ), and both outperform the AK135 model ( $N_{win} = 347$ ,  $N_{traces} = 247$ ). Our overall assessment for the Qeshm event is that both 3-D models outperform the AK135 model and it is difficult to conclude that either 3-D model clearly predicts waveforms more effectively than the other for this event and in these period bands.

### 5.3 Results for the 2017 $M_w = 5.21$ DPRK declared nuclear test

On 2017 September 3, the DPRK announced the detonation of their 6th underground nuclear explosives test. The test had the largest moment magnitude of all six declared tests ( $M_w = 5.21$ , Chiang *et al.* 2018). The event was well recorded by multiple regional networks and stations, as well as several GSN and GEOSCOPE stations in the region. These include several stations in Japanese networks (F-net, Bosai-Ken Network and Japan Meteorological Agency network), the Hong Kong Seismic Network, the Broadband Array in Taiwan

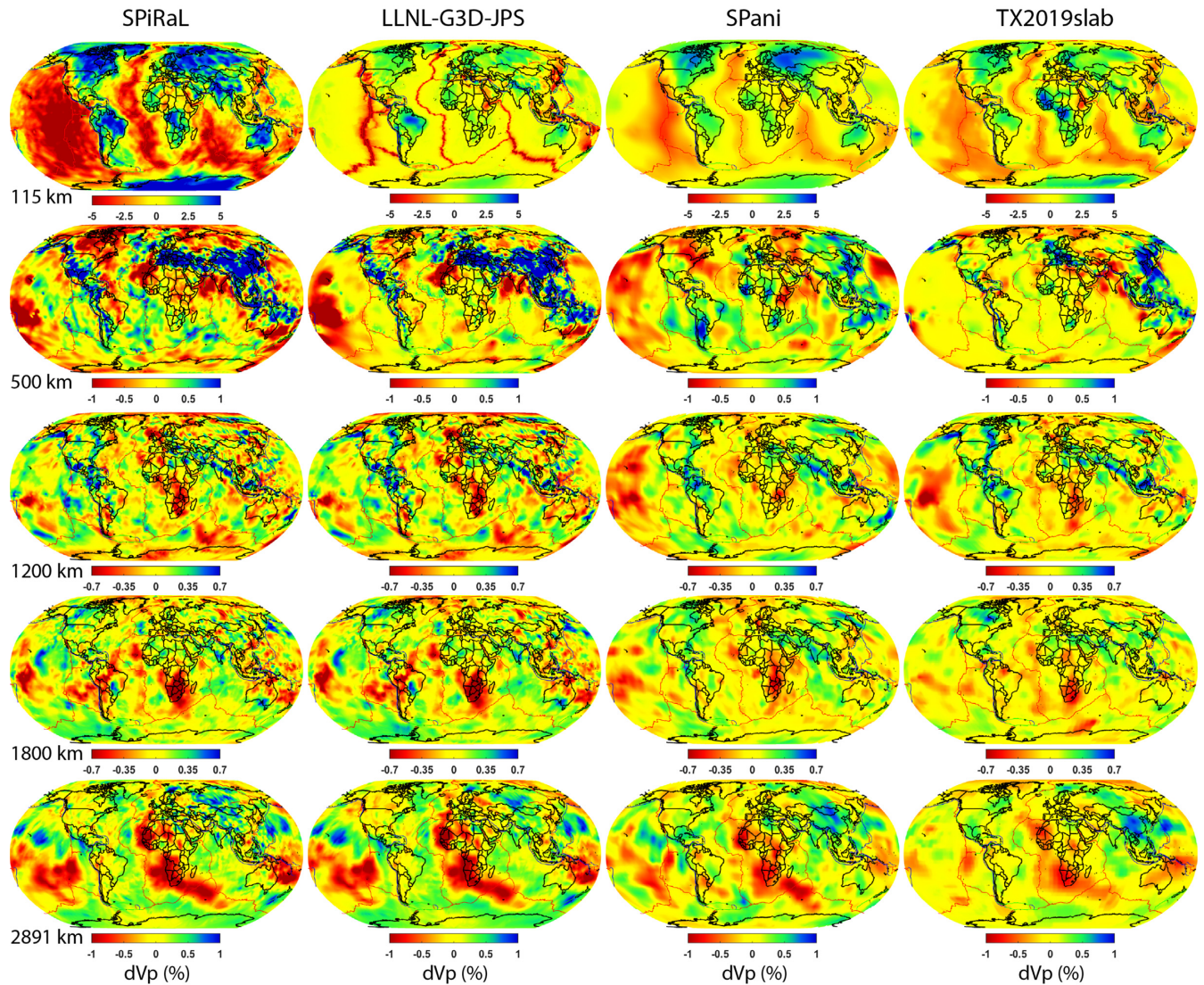


**Figure 13.** Comparison of SPiRaL  $V_p$  anomalies to other selected joint  $V_p$ - $V_s$  models. LLNL-G3D-JPS (Simmons *et al.* 2015), SPani (Tesoniero *et al.* 2015) and TX2019slab (Lu *et al.* 2019).

**Table 4.** Seismic events used in full waveform simulations.

Event	Date/Time	Lat	Lon	depth (km)	$M_{xx}$	$M_{yy}$	$M_{zz}$	$M_{xy}$	$M_{xz}$	$M_{yz}$	$M_0$	$M_w$	MT method	MT source
Wells (Nevada)	2008/02/21 14:16:05	41.08N	114.77W	11	202	673	-874	-373	19.9	-161	891	5.9	RMT	USGS/SLU
Qeshm (Iran)	2005/11/27 10:22:55.86	26.77N	55.86E	10	-1030	76	952	-165	226	-40	1740	6.1	CMT	GCMT
DPRK6 (North Korea)	2017/09/03 03:30:01.68	41.30N	129.08E	0.6	66.3	65.3	70.3	-10.3	2	5	80.6	5.21	RMT	Chiang <i>et al.</i> (2018)

Notes: All seismic moment ( $M_{ij}$ ,  $M_0$ ) terms are in  $1e15$  N-m. DPRK6 hypocentre from Myers *et al.* (2018).

MT = Moment Tensor; RMT = Regional Moment Tensor; CMT = Centroid Moment Tensor; USGS = United States Geological Survey; SLU = Saint Louis University; GCMT = Global Centroid Moment Tensor project

for Seismology, Regional Integrated Multi-Hazard Early Warning System in Thailand, Marianas Islands (USGS) and the Korea National Seismic Network. In total, we simulated waveforms to 114 stations in the region using SPiRaL, AK135 and the FWEA18 model (Tao *et al.* 2018). FWEA18 is a high-resolution model of East Asia, based on full-waveform tomography using a large collection of data recorded at multiple dense regional networks in China, Japan, Korea, Mongolia and other parts of East Asia. The study considered events occurring between 2009 and 2016, therefore did not include the 2017 DPRK declared nuclear test. FWEA18 was constructed

by fitting body waveforms in the period band of 8–100 seconds and surface waveforms in the period band of 40–100 s. They applied an adjoint simulation method to construct model gradients to perform the inversion (e.g. Tromp *et al.* 2005; Fichtner *et al.* 2006).

Example waveforms for the DPRK6 event are shown in Fig. 20 for station ENH at a distance of 2146 km in eastern China and in Fig. S9 in the Supporting Information for station KNP at 1232 km away in Japan. Our qualitative (visual) assessment of the data and synthetic comparisons show that the SPiRaL model clearly predicts the waveforms better than the 1-D AK135 model overall and is at

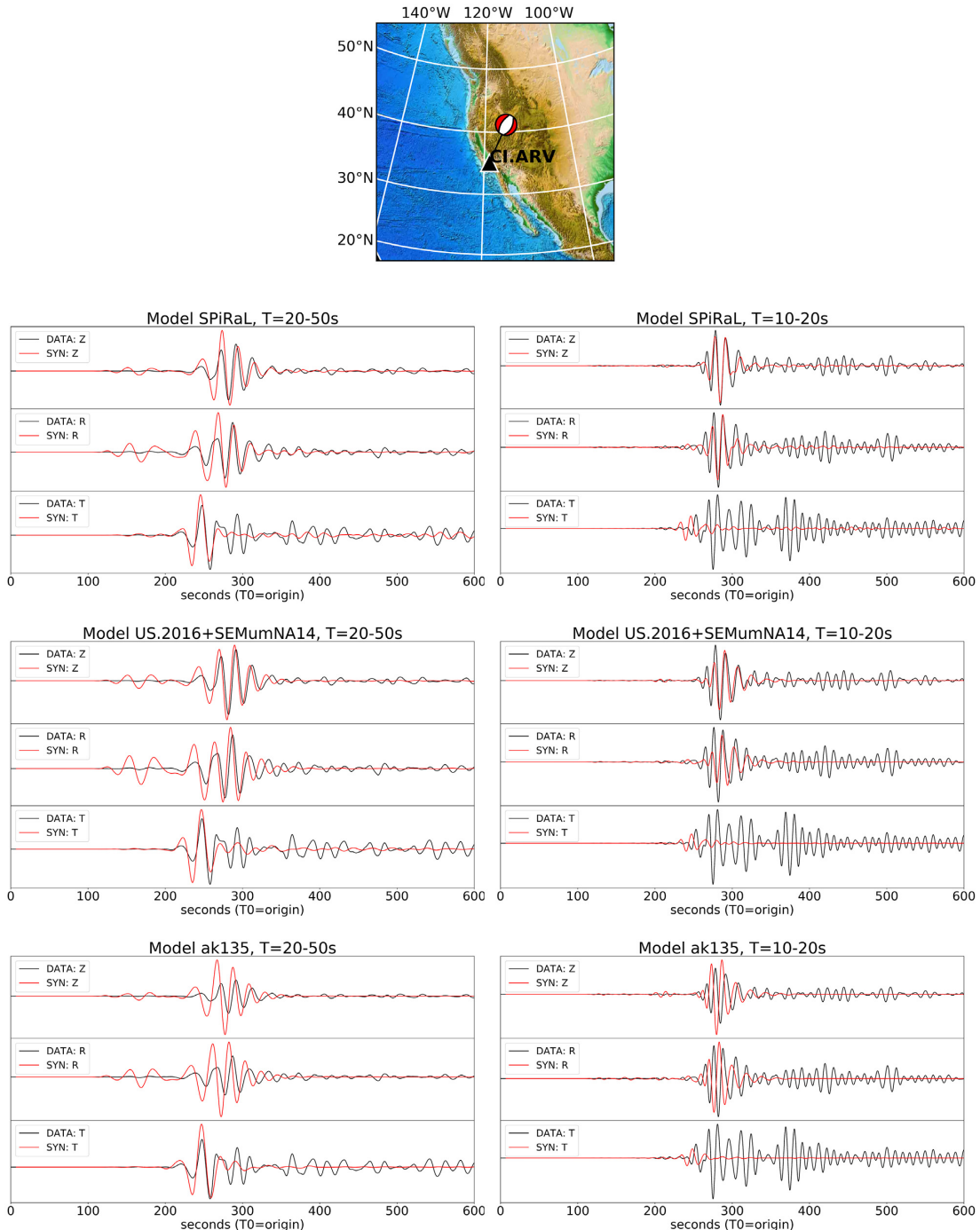


**Figure 14.** Displacement waveform data (black lines) and SPECFEM3D.Globe simulations (red lines) for the 2008 Wells, Nevada earthquake ( $M_w = 5.9$ ) recorded at station ARV in the Southern California Seismic Network. Waveforms are shown for SPiRaL, US.2016+SEMuNA14 (Yuan *et al.* 2014; Shen & Ritzwoller 2016) and AK135 (Kennett *et al.* 1995) models in the 20–50 and 10–20 s period bands as labelled. See Fig. S7 in the Supporting Information for more simulations.

least on par with the FWEA18 model in both period bands (20–50 and 10–20 s). However, close visual inspection indicates that the FWEA18 tends to predict *S* body waveforms better than SPiRaL at the longer distances (>2000 km). Like the other events, our qualitative (visual) assessment is supported by the Pyflex window picking analysis (Figs 21 and 22). In the 20–50 s period band, slightly more windows are selected with SPiRaL ( $N_{win} = 271$ ,  $N_{traces} = 221$ ) compared to FWEA18 ( $N_{win} = 234$ ,  $N_{traces} = 180$ ). Both 3-D models predict waveforms far better than AK135

overall ( $N_{win} = 78$ ,  $N_{traces} = 60$ ), but we point out that this result is somewhat biased because AK135 is not suitable for paths to Japan that traverse the oceanic crust in the Sea of Japan. We note that paths to Japan and other islands are important for monitoring seismic events in the region and accurate prediction of waveforms is highly desirable for source inversion and other applications. All models tend to show sharp degradation in fits in the 10–20 period band, as shown in the example waveforms (Fig. 20). Nonetheless, in the 10–20 period band (Fig. 22) the Pyflex selects more windows

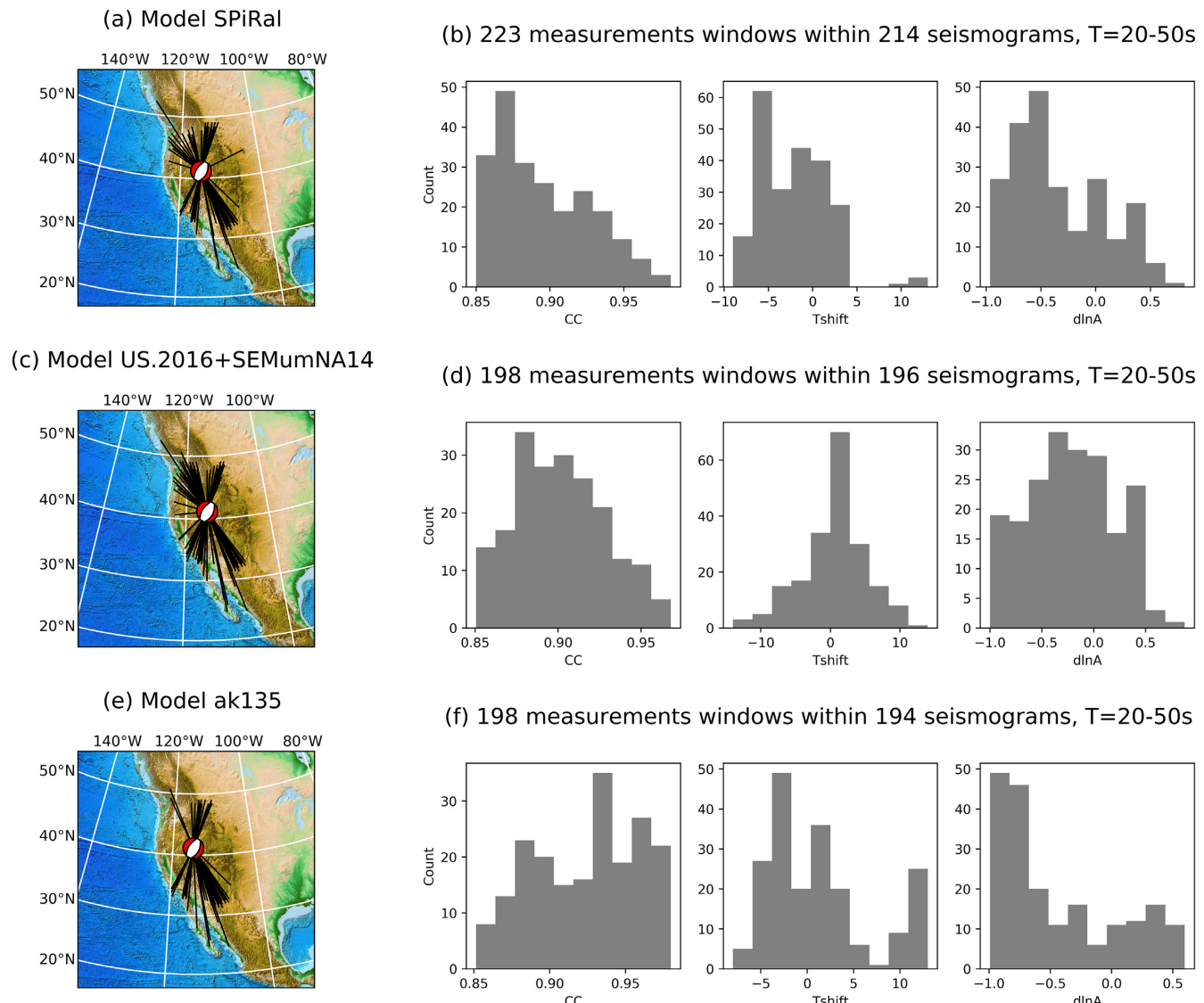


**Figure 15.** Pyflex automatic data/synthetic window picking metrics for the 2008 Wells, Nevada earthquake in the period band of 20–50 s. (a) Event-station path map for picked windows using the SPIRAL model. (b) Cross correlation (CC), phase time-shift in seconds ( $T_{shift}$ ) and amplitude difference ( $d\ln A$ ) distributions using SPIRAL (223 picked windows). (c) and (d) Same as top row except for the US.2016+SEMuNA14 model (198 picked windows). (e) and (f) Same as top row except for the AK135 model (198 picked windows).

when the SPIRAL model is used ( $N_{win} = 214$ ,  $N_{traces} = 161$ ) than when the FWEA18 is used ( $N_{win} = 155$ ,  $N_{traces} = 129$ ). Pyflex selects even fewer window when the AK135 model is used ( $N_{win} = 132$ ,  $N_{traces} = 116$ ). We also note that the distribution of the time-shifts ( $T_{shift}$ ) and amplitude differences ( $d\ln A$ ) are well centred about zero for SPIRAL-based waveforms. Although there is sample bias that over weights stations in Japan, we conclude that the SPIRAL model predicts waveforms more accurately than AK135 and similarly to the FWEA18 model for this particular event and period bands.

## 6 DISCUSSION AND CONCLUSIONS

We constructed a new global-scale model (SPIRAL) of the crust and mantle based on body wave traveltimes (local, regional and teleseismic phases) and surface wave dispersion maps (25–200 s

period range). SPIRAL is a relatively high-resolution model with refined grids down to  $\sim 0.25^\circ$  node spacing in the crust and shallow upper mantle. SPIRAL includes seven crustal units, undulating discontinuities, ellipticity and mantle stretching, and it is composed of  $> 2$  million model nodes. SPIRAL also includes 3-D variations of VTI parameters throughout the crust and mantle. Since we considered both  $P$  and  $S$  waves travelling in arbitrary directions, we attempted to model five VTI parameters defined by Thomsen (1986) at each node. Overall, we find velocity variation amplitudes in the shallow upper mantle that tend to be stronger than other global models, and additional details are seen for commonly observed velocity anomaly patterns. We find that the lower mantle velocity structures in SPIRAL are largely unchanged from the starting model (LLNL-G3D-JPS, Simmons et al. 2015), which was based on a large subset of the body waves that were used in this study.

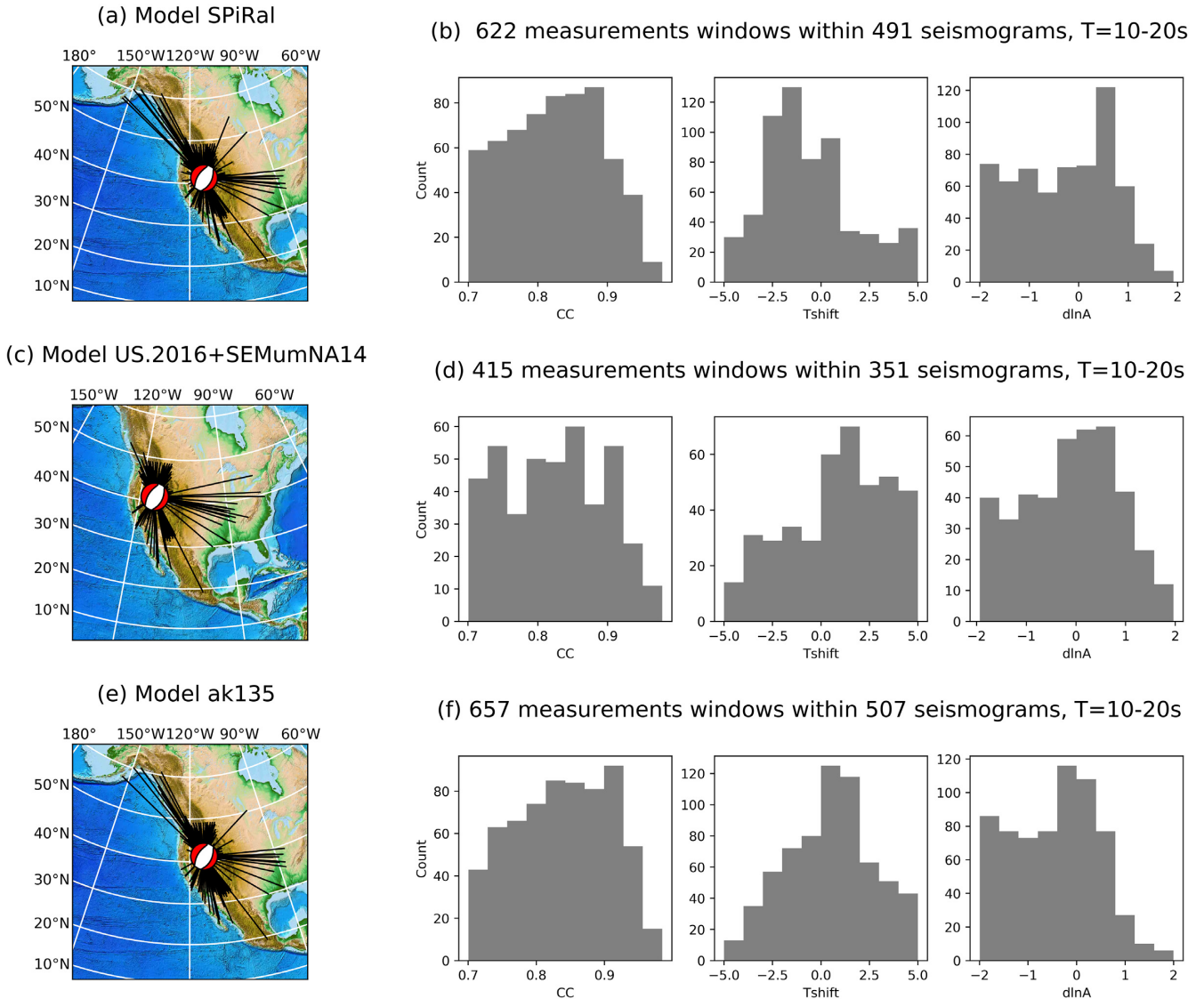


**Figure 16.** Pyflex automatic data/synthetic window picking metrics for the 2008 Wells, Nevada earthquake in the period band of 10–20 s. (a) Event-station path map for picked windows using the SPiRaL model. (b) Cross correlation (CC), phase time-shift in seconds ( $T_{shift}$ ) and amplitude difference ( $d\ln A$ ) distributions using SPiRaL (622 picked windows). (c) and (d) Same as top row except for the US.2016+SEMuNA14 model (415 picked windows). (e) and (f) Same as top row except for the AK135 model (657 picked windows).

Our nonlinear modelling approach provides some constraints on the coupling between  $V_p$  and  $V_s$  perturbations at each iteration, however that constraint is not strictly enforced and the additive effects of each iteration may drive  $V_p:V_s$  away from expected thermal values. As a result, we find that  $V_p$  and  $V_s$  anomalies tend to diverge from expected thermal variations in the shallowest upper mantle beneath the oceans. In these regions,  $V_p$  tends to be slow with asymmetric patterns about mid-ocean ridge axes (most notably, the East Pacific Rise). Interestingly, Tesoniero *et al.* (2015) also noted this behaviour when  $V_p-V_s$  coupling was relaxed in a test model. In the shallowest upper mantle beneath the ocean basins,  $V_p:V_s$  ratios in SPiRaL are  $\sim 1.65$ – $1.70$  which is consistent with un-serpentinized upper-mantle peridotite (Holbrook *et al.* 1992). Similar values have been observed in detailed OBS studies beneath the Jan Mayen Ridge region for example (Mjelde *et al.* 2007; Kandilarov *et al.* 2015). Given the expected and independently observed strong non-thermal effects in the shallowest upper mantle, we deem our results to be plausible but we urge caution when interpreting.

Unlike continental regions, the upper mantle  $V_p$  beneath the oceans is only weakly constrained by body waves and the sensitivity of Rayleigh waves to  $V_p$  and the potential for trade-off with  $V_s$  and anisotropy parameters is significant. As a test, we fixed the upper mantle  $V_p$  of SPiRaL to conform to an average  $V_p:V_s$  and computed the impact on the resulting dispersion curves at several points in the Pacific Ocean where the lowest  $V_p:V_s$  anomalies are observed (Fig. S10, Supporting Information). This simple test shows the small (but notable) impact of  $V_p$  on the dispersion curves. We also note that a poor reference (starting) model for  $V_p$  in the uppermost mantle could lead to artefacts beneath the oceans (e.g. Ritsema & van Heijst 2002). More detailed studies that consider alternative starting models and incorporation of additional data in future inversions (e.g. PP waves and/or OBS data) will provide important constraints on this region. Body wave sampling (hit count) maps are provided in Figs S1–S3 (Supporting Information) for guidance on the degree of uncertainty that should be considered throughout the entire model.

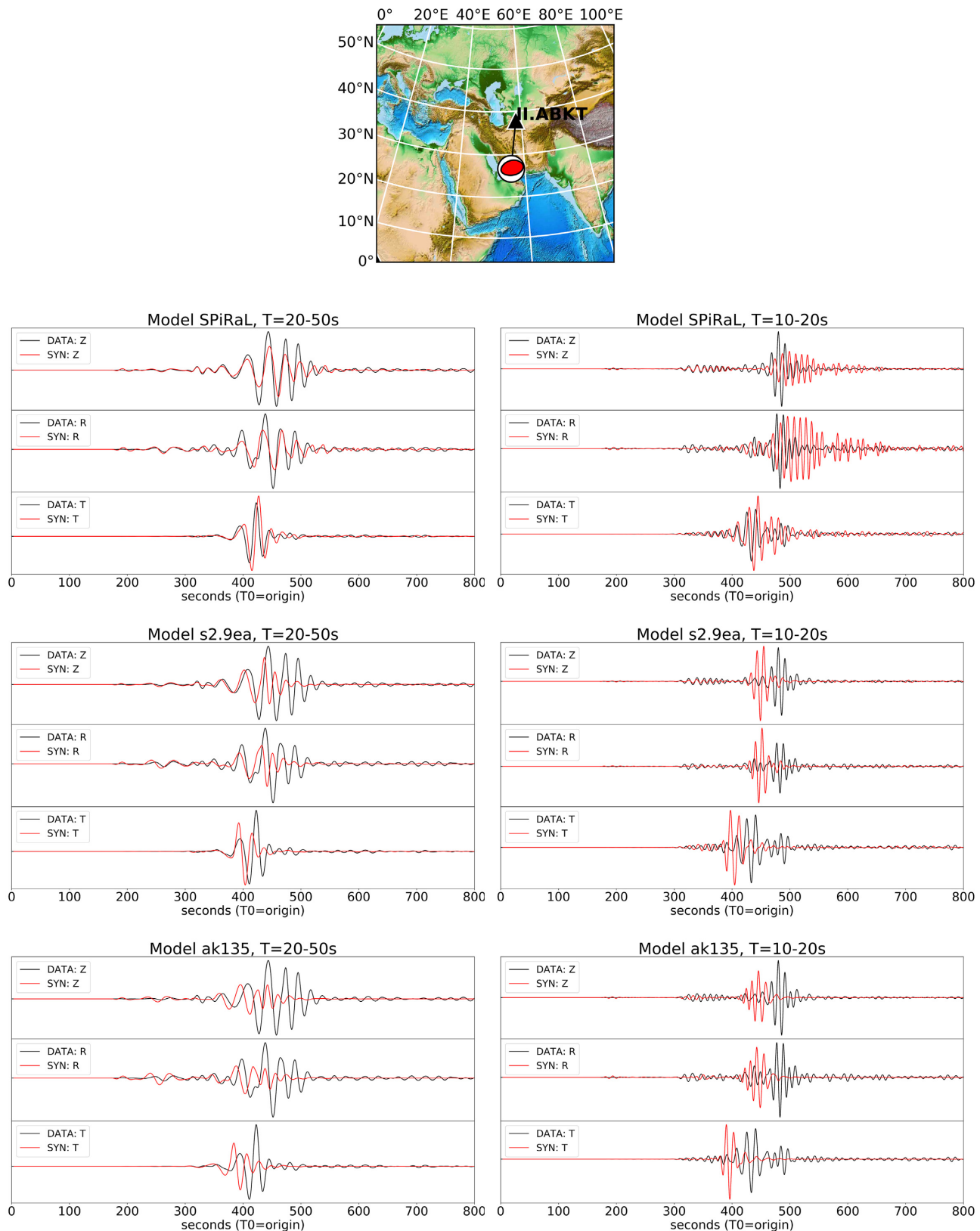


**Figure 17.** Displacement waveform data (black lines) and SPECFEM3D\_Globe simulations (red lines) for the 2005 Qeshm, Iran earthquake ( $M_w = 6.1$ ) recorded at station ABKT in Turkmenistan. Waveforms are shown for SPiRaL, S2.9EA (Kustowski *et al.* 2008) and AK135 models in the 20–50 and 10–20 s period bands as labelled. See Fig. S8 in the Supporting Information for more simulations.

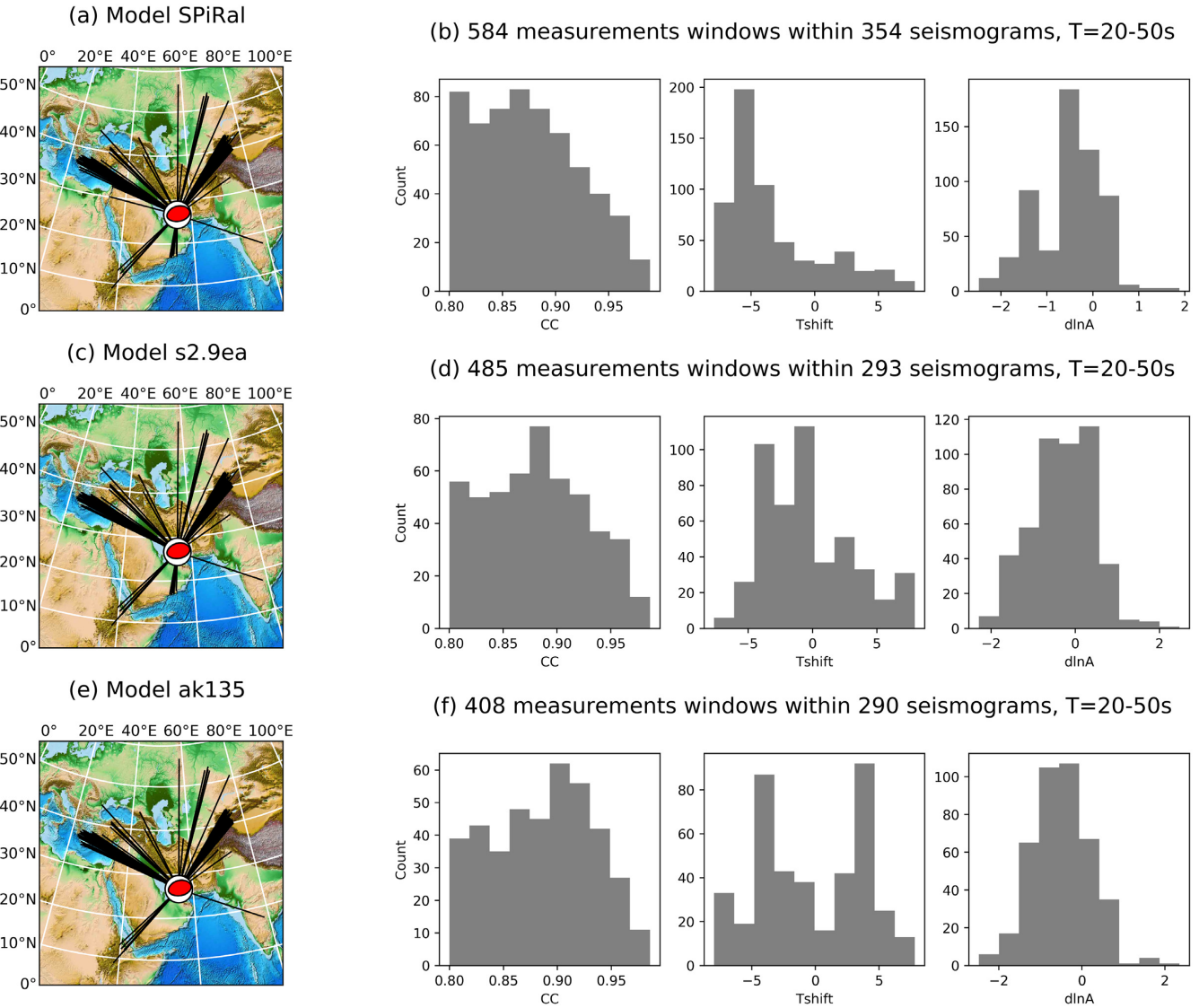


**Figure 18.** Pyflex automatic data/synthetic window picking metrics for the 2005 Qeshm, Iran earthquake in the period band of 20–50 s. (a) Event-station path map for picked windows using the SPiRaL model. (b) Cross correlation (CC), phase time-shift in seconds ( $T_{shift}$ ) and amplitude difference ( $dlnA$ ) distributions using SPiRaL (584 picked windows). (c) and (d) Same as top row except for the S2.9EA model (485 picked windows). (e) and (f) Same as top row except for the AK135 model (408 picked windows).

The intensity of the shear wave anisotropy (VTI) is found to be significantly stronger than compressional wave anisotropy overall, with  $Vsh/Vsv$  exceeding 1.04 in some areas within the shallow upper mantle (i.e.  $Vsh$  that is 4 per cent faster than  $Vsv$ ). Between the Moho and  $\sim 250$  km depth,  $Vsh/Vsv$  is almost always positive ( $Vsh > Vsv$ ) and abruptly shifts to neutral ( $Vsh \approx Vsv$ ) below these depths (Fig. 8). This overall result is consistent with several other previous studies, however there is significant 3-D variability suggesting that a 1-D treatment of anisotropy may not be sufficient for global-scale studies that include Rayleigh and Love waves (see Fig. 8). The intensity of the compressional anisotropy tends to be much smaller than shear anisotropy; however, some patterns emerge including positive  $Vpv/Vph$  ratios beneath the continents and negative  $Vpv/Vph$  ratios beneath oceans in the shallowest upper mantle. Deeper down ( $\sim 150$  km), the behavior tends to shift to positive  $Vpv/Vph$  beneath the oceans (Fig. 7).

We are reluctant to interpret the compressional anisotropy results since they are only weakly constrained by the data overall, which

was astutely pointed out by Tesoniero *et al.* (2015). Another important limitation of this study is the assumption that anisotropy is strictly VTI without regard for azimuthal or more general forms of anisotropy. While our primary concern was reconciling the radial anisotropy effects that lead to large discrepancies between Love and Rayleigh wave velocities, we note the potential for imaging artifacts that may result from assuming the simplified anisotropy system (e.g. Sieminski *et al.* 2007; Bezada *et al.* 2016; Beller & Chevrot 2020). The potential for artifacts is notably problematic in complex regions such as subduction zones where it has been recommended to prescribe anisotropy fields derived from geodynamic modelling rather than inverting for the parameters in body wave tomography (Bezada *et al.* 2016).

We explore the value of the high-resolution SPiRaL (or similar) model as a starting point for FWI. We propose that starting with such a traveltime-based model may accelerate our long-term objective to construct a global-scale model capable of predicting waveforms including periods of  $<<20$  s over broad areas (1000–3000 km) or

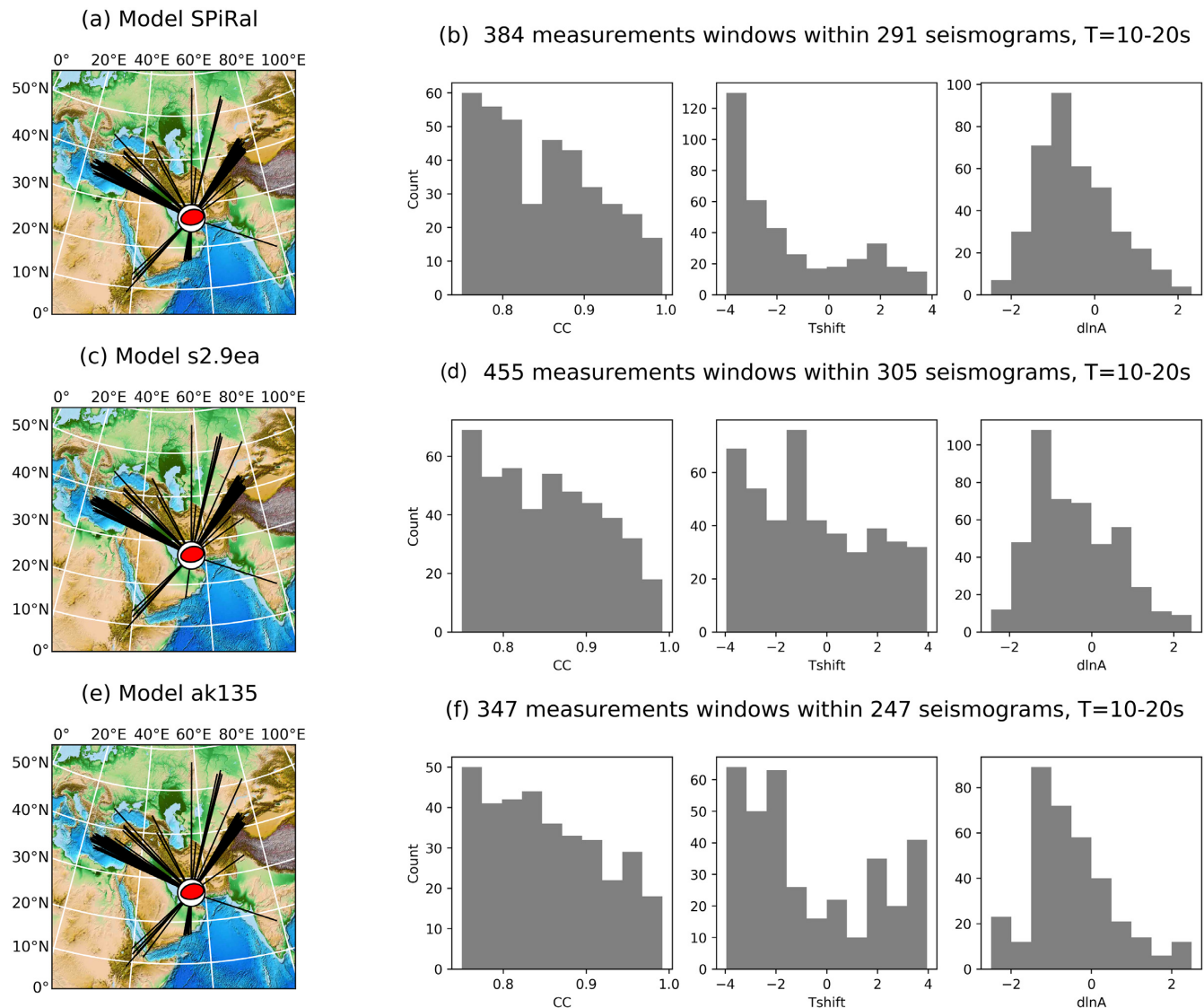


**Figure 19.** Pyflex automatic data/synthetic window picking metrics for the 2005 Qeshm, Iran earthquake in the period band of 10–20 s. (a) Event-station path map for picked windows using the SPiRaL model. (b) Cross correlation (CC), phase time-shift in seconds ( $T_{shift}$ ) and amplitude difference ( $d\ln A$ ) distributions using SPiRaL (384 picked windows). (c) and (d) Same as top row except for the S2.9EA model (455 picked windows). (e) and (f) Same as top row except for the AK135 model (347 picked windows).

perhaps globally, while maintaining the ability to predict accurate traveltimes at regional and teleseismic distances. We performed full waveform simulations using SPiRaL and a selection of regional models to benchmark the waveform prediction performance of SPiRaL in a few key regions using some simple statistical measures described herein. Overall, these results show that SPiRaL performs equally well as the selected independent waveform-based models for these events in the evaluated period range of 10–50 s. This suggests that SPiRaL may serve as a starting model for FWI with a target of predicting waves in this period band over the broad regions considered. We recognize that only a small number of events were simulated over a limited distance range in this study and more simulations and analyses are needed to evaluate the suitability of SPiRaL to serve as a starting model for FWI in other regions and perhaps globally.

Our emphasis here is on waveform periods that are most significant to monitoring (10–50 s), we note that FWI on the global scale should also consider longer period waves (perhaps up to 200 s) as

well. Typical FWI approaches progress from these longer periods down to shorter periods to refine the models. If a similar global approach is taken with SPiRaL as a starting model, effort should be made to preserve the short-scale details in the shallow upper mantle (<200 km) through this progression. The preservation of such details provided by the classical traveltime inversion should minimize the number of iterations needed to fit the shorter period waveforms (<<50 s) which are more computationally intensive than longer period (>50 s) simulations/inversions. A possible approach is iterative inversions involving FWI model updates followed by classical traveltime inversion with the same or similar data/methods used to construct SPiRaL.

Our progression of global model development has followed the guidance in Zucca *et al.* (2009) where experts laid out an effective direction forward for constructing 3-D models that addressed near- and long-term societal needs including improved seismic event monitoring. Our previous global models (LLNL-G3Dv3, Simmons *et al.* 2012; LLNL-G3D-JPS, Simmons *et al.* 2015) were

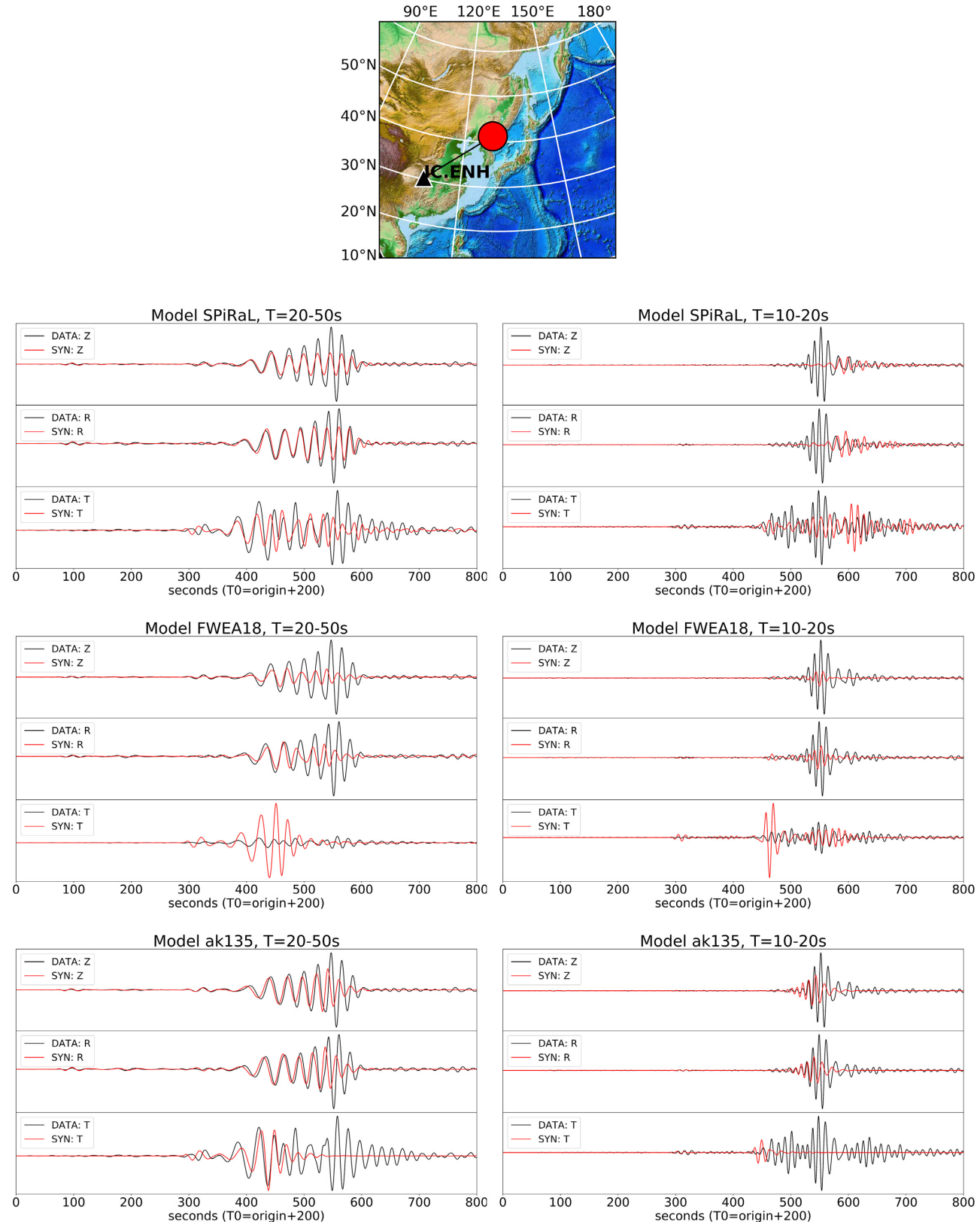


**Figure 20.** Displacement waveform data (black lines) and SPECFEM3D\_Globe simulations (red lines) for the 2017 DPRK declared nuclear explosion ( $M_w = 5.21$ ) recorded at station ENH in eastern China. Waveforms are shown for SPiRaL, FWEA18 (Tao *et al.* 2018) and AK135 models in the 20–50 and 10–20 s period bands as labelled. See Fig. S9 in the Supporting Information for more simulations.

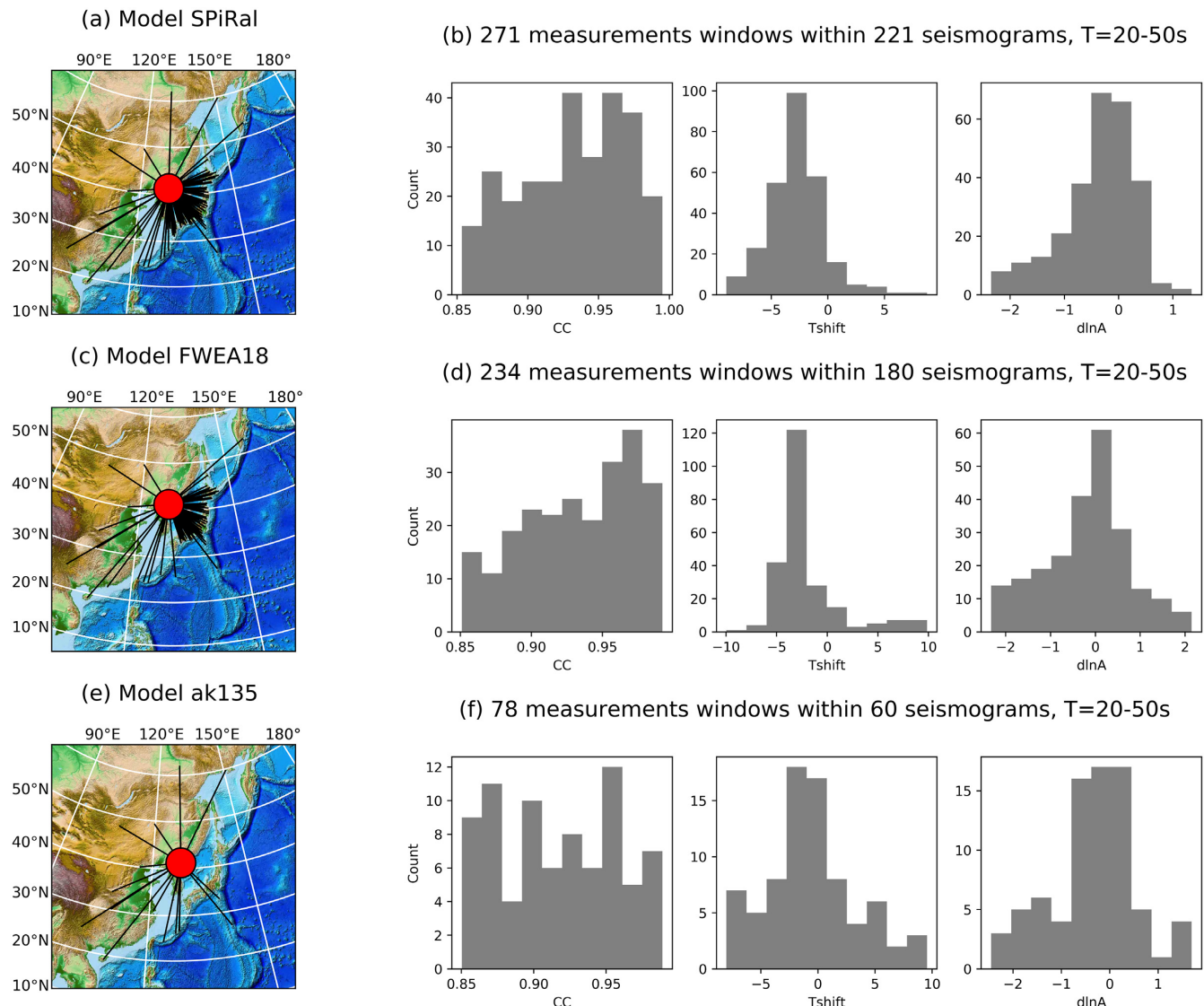


**Figure 21.** Pyflex automatic data/synthetic window picking metrics for the 2017 DPRK declared nuclear test in the period band of 20–50 s. (a) Event-station path map for picked windows using the SPiRaL model. (b) Cross correlation (CC), phase time-shift in seconds ( $T_{\text{shift}}$ ) and amplitude difference ( $d\ln A$ ) distributions using SPiRaL (271 picked windows). (c) and (d) Same as top row except for the FWEA18 model (234 picked windows). (e) and (f) Same as top row except for the AK135 model (78 picked windows).

constructed with crustal, regional and teleseismic traveltimes data sets with a goal of improving event location. These models have been shown to be useful for improved seismic event location without regional traveltimes error contamination due to strong upper mantle 3-D heterogeneities (Myers *et al.* 2015). The SPiRaL model represents the next phase in our effort to construct 3-D models (global scale in this case) for source characterization that not only predict accurate traveltimes for seismic event location, but also long-period surface wave dispersion with a single- and self-consistent model.

While traveltimes and surface wave dispersion may be predicted well with separate models optimized for each type of observable, the combination of the two should lead to models that more closely represent the Earth. This assertion holds even more merit if a wide spectrum of scale-lengths of heterogeneity are represented. Although the increased seismic monitoring benefit of the SPiRaL model is not fully realized, we believe the model does provide a valuable starting

model for further refinement over broad regions of interest (likely involving waveform inversion). Thus, SPiRaL could prove useful in addressing current monitoring challenges including the improved prediction of waveforms with periods under 20 s at distances ranging from hundreds to a few thousand kilometres from an event. Such prediction capabilities will help characterize/categorize small events ( $M < 4$ ) that produce less long period energy.

## ACKNOWLEDGEMENTS

We thank the editor and two anonymous reviewers for their insightful comments and suggestions that greatly improved this paper. Sung-Joon Chang at Kangwon National University for sharing anisotropy profiles. Min Chen and Tong Zhou at Michigan State University kindly shared the US2016 and SEMumNA14 models in a simulation-ready format. Kai Tao, Steve Grand and Chu-jie Liu at The University of Texas at Austin gratefully provided

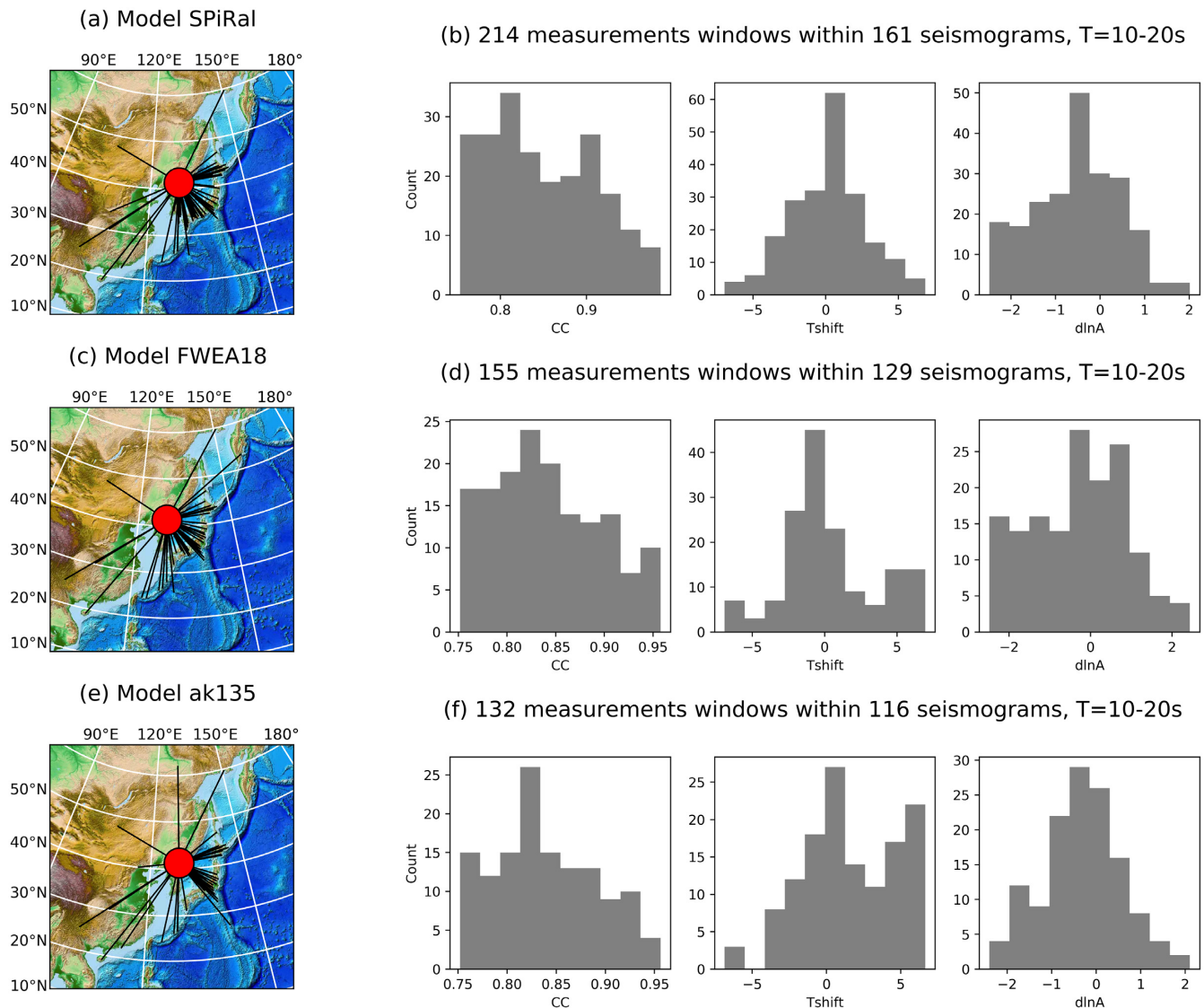


**Figure 22.** Pyflex automatic data/synthetic window picking metrics for the 2017 DPRK declared nuclear test in the period band of 10–20 s. (a) Event-station path map for picked windows using the SPiRaL model. (b) Cross correlation ( $CC$ ), phase time-shift in seconds ( $T_{shift}$ ) and amplitude difference ( $dlnA$ ) distributions using SPiRaL (214 picked windows). (c) and (d) Same as top row except for the FWEA18 model (155 picked windows). (e) and (f) Same as top row except for the AK135 model (132 picked windows).

the FWEA18 model in a simulation-ready format. Data were provided by the Incorporated Research Institutions for Seismology (IRIS) Data Management Center (DMC) (<https://ds.iris.edu/ds/nodes/dmc/>), the International Seismological Centre (ISC) (<http://www.isc.ac.uk>), the United States Geological Survey (USGS) National Earthquake Information Center (NEIC) ([www.usgs.gov](http://www.usgs.gov)) and Japan's Broadband Seismographic Network (F-net) (<https://www.fnet.bosai.go.jp/>). Waveform simulations were performed with SPECFEM3D\_Globe ([https://geodynamics.org/cig/software/specfem3d\\_globe/](https://geodynamics.org/cig/software/specfem3d_globe/)) on LLNL's Quartz supercomputer (<https://hpc.llnl.gov/hardware/platforms/Quartz>). Seismic waveform processing and analysis were performed with ObsPy (<https://docs.obspy.org>) and Pyflex (<https://krischer.github.io/pyflex/>). Surface wave dispersion predictions and sensitivity kernels were computed using the senskernel-1.0 package provided by Colorado University Boulder (<https://github.com/NoiseCIEI/SensKernel>). This work was performed under the auspices of the U.S. Department of Energy by Lawrence Livermore National Security, LLC, Lawrence Livermore

National Laboratory under Contract DE-AC52-07NA27344. This research was funded by the National Nuclear Security Administration's Office of Defense Nuclear Nonproliferation Research and Development LLNL-JRNL-814523.

## DATA AVAILABILITY STATEMENT

The data underlying this article will be shared on reasonable request to the corresponding author.

## REFERENCES

- Afanasiev, M., Peter, D., Sager, K., Simutė, S., Ermert, L., Krischer, L. & Fichtner, A., 2016. Foundations for a multiscale collaborative global Earth model, *Geophys. J. Int.*, **204**, 39–58.
- Alessandrini, B., 1989. The hydrostatic equilibrium figure of the Earth: an iterative approach, *Phys. Earth planet. Inter.*, **54**, 180–192.
- Auer, L., Boschi, L., Becker, T.W., Nissen-Meyer, T. & Giardini, D., 2014. Savani: a variable resolution whole-mantle model of anisotropic shear

- velocity variations based on multiple data sets. *J. geophys. Res.*, **119**, 3006–3034.
- Ballard, S., Hipp, J.R., Begnaud, M.L., Young, C.J., Encarnacao, A.V., Chael, E.P. & Phillips, W.S., 2016. SALSA3D: a tomographic model of compressional wave slowness in the Earth's mantle for improved travel-time prediction and travel-time prediction uncertainty, *Bull. seism. Soc. Am.*, **106**(6), 2900–2916.
- Beller, S. & Chevrot, S., 2020. Probing depth and lateral variations of upper-mantle seismic anisotropy from full-waveform inversion of teleseismic body-waves, *Geophys. J. Int.*, **222**(1), 352–387.
- Bezada, M.J., Faccenda, M. & Toomey, D.R., 2016. Representing anisotropic subduction zones with isotropic velocity models: a characterization of the problem and some steps on a possible path forward, *Geochem. Geophys. Geosyst.*, **17**, 3164–3189.
- Bodin, T. & Sambridge, M., 2009. Seismic tomography with the reversible jump algorithm. *Geophys. J. Int.*, **178**, 1411–1436.
- Boschi, L., Fry, B., Ekström, G. & Giardini, D., 2009. The European upper mantle as seen by surface waves. *Surv. Geophys.*, **30**, 463–501.
- Bozdag, E.D.P., Lefebvre, M., Komatitsch, D., Tromp, J., Hill, J., Podhorszki, N. & Pugmire, D., 2016. Global adjoint tomography: first-generation model, *Geophys. J. Int.*, **207**(3), 1739–1766.
- Chang, S.-J., Ferreira, A.M.G., Ritsema, J., van Heijst, H.J. & Woodhouse, J.H., 2015. Joint inversion for global isotropic and radially anisotropic mantle structure including crustal thickness perturbations, *J. geophys. Res.*, **120**, 4278–4300.
- Chiang, A., Ichinose, G.A., Dreger, D.S., Ford, S.R., Matzel, E.M., Myers, S.C. & Walter, W.R., 2018. Moment tensor source-type analysis for the Democratic People's Republic of Korea—declared nuclear explosions (2006–2017) and 3 September 2017 collapse event. *Seismol. Res. Lett.*, **89**(6), 2152–2165.
- Cupillard, P., Delavaud, E., Burgos, G., Festa, G., Villette, J.-P., Capdeville, Y. & Montagner, J.-P., 2012. RegSEM: a versatile code based on the spectral element method to compute seismic wave propagation at the regional scale. *Geophys. J. Int.*, **188**, 1203–1220.
- Durand, S., Debayle, E., Ricard, Y., Zaroli, C. & Lambotte, S., 2017. Confirmation of a change in the global shear velocity pattern at around 1,000 km depth, *Geophys. J. Int.*, **211**(3), 1628–1639.
- Dziewonski, A.M. & Anderson, D.L., 1981. Preliminary reference Earth model, *Phys. Earth planet. Inter.*, **25**, 297–356.
- Fichtner, A., Bunge, H.P. & Igel, H., 2006. The adjoint method in seismology—II. Applications: traveltimes and sensitivity functionals, *Phys. Earth planet. Inter.*, **157**(1–2), 105–123.
- Fichtner, A. et al., 2018. The Collaborative Seismic Earth Model: generation 1. *Geophys. Res. Lett.*, **45**(9), 4007–4016.
- French, S., Lekic, V. & Romanowicz, B., 2013. Waveform tomography reveals channeled flow at the base of the oceanic asthenosphere, *Science*, **342**, 227–230.
- French, S.W. & Romanowicz, B., 2015. Broad plumes rooted at the base of the earth's mantle beneath major hotspots, *Nature*, **525**(7567), 95–99.
- Grand, S.P., Van der Hilst, R.D. & Widjiantoro, S., 1997. Global seismic tomography: a snapshot of convection in the Earth. *GSA Today*, **7**(4), 1–7.
- Grand, S.P., 2002. Mantle shear-wave tomography and the fate of subducted slabs, *Philos. Trans. R. Soc. Lond. A*, **360**(1800), 2475–2491.
- Grevemeyer, I., Ranero, C.R. & Ivandic, M., 2018. Structure of oceanic crust and serpentinitization at subduction trenches, *Geosphere*, **14**(2), 395–418.
- Holbrook, W.S., Mooney, W.D. & Christensen, N.J., 1992. Seismic velocity structure of the deep continental crust. In: Fountain, D., Arculus, R. & Kay, R.W.(eds) *Continental Lower Crust*. Elsevier, Amsterdam, pp 451–464.
- Hosseini, K., Sigloch, K., Tsekhnistrenko, M., Zaheri, A., Nissen-Meyer, T. & Igel, H., 2020. Global mantle structure from multifrequency tomography using P, PP and P-diffracted waves, *Geophys. J. Int.*, **220**(1), 96–141.
- Ishii, M. & Tromp, J., 1999. Normal-mode and free-air gravity constraints on lateral variations in velocity and density of Earth's mantle, *Science*, **285**(5431), 1231–1236.
- Kandilarov, A., Mjelde, R., Flueh, E. & Pedersen, R.B., 2015. Vp/Vs-ratios and anisotropy on the northern Jan Mayen Ridge, North Atlantic, determined from ocean bottom seismic data, *Polar Sci.*, **9**(3), 293–310.
- Kennett, B.L.N., Engdahl, E.R. & Buland, R., 1995. Constraints on seismic velocities in the earth from travel times. *Geophys. J. Int.*, **122**, 108–124.
- Koelemeijer, P., Ritsema, J., Deuss, A. & van Heijst, H.-J., 2016. SP12RTS: a degree-12 model of shear- and compressional-wave velocity for Earth's mantle, *Geophys. J. Int.*, **204**, 1024–1039.
- Komatitsch, D. & Tromp, J., 2002a. Spectral-element simulations of global seismic wave propagation-I. Validation, *Geophys. J. Int.*, **149**(2), 390–412.
- Komatitsch, D. & Tromp, J., 2002b. Spectral-element simulations of global seismic wave propagation-II. Three-dimensional models, oceans, rotation and self-gravitation, *Geophys. J. Int.*, **150**(1), 303–318.
- Komatitsch, D. et al., 2015. SPECFEM3D GLOBE v7.0.0 [software], Computational Infrastructure for Geodynamics. [https://geodynamics.org/cig/software/specfem3d\\_globe/](https://geodynamics.org/cig/software/specfem3d_globe/).
- Krischer, L. & Casarotti, E., 2015. pyflex: 0.1.4 (Version 0.1.4). Zenodo. <http://doi.org/10.5281/zenodo.31607>
- Kustowski, B., Ekström, G. & Dziewoski, A.M., 2008. The shear-wave velocity structure in the upper mantle beneath Eurasia, *Geophys. J. Int.*, **174**, 978–992.
- Laske, G., Masters, G., Ma, Z. & Pasquano, M., 2013. Update on CRUST1.0 – A 1-degree Global Model of Earth's Crust, *Geophys. Res. Abstr.*, **15**, Abstract EGU2013–2658.
- Lawrence, J. & Shearer, P., 2008. Imaging mantle transition zone thickness with SdS-SS finite-frequency sensitivity kernels. *Geophys. J. Int.*, **174**(1), 143–158.
- Lei, W. et al., 2020. Global adjoint tomography-model GLAD-M25, *Geophys. J. Int.*, **233**, 1–21.
- Li, X.-D. & Romanowicz, B., 1996. Global mantle shear velocity model developed using nonlinear asymptotic coupling theory, *J. geophys. Res.*, **101**(B10), 22,245–22,272.
- Lu, C. & Grand, S.P., 2016. The effect of subducting slabs in global shear wave tomography, *Geophys. J. Int.*, **205**(2), 1074–1085.
- Lu, C., Grand, S.P., Lai, H. & Garnero, E.J., 2019. TX2019slab: a new P and S tomography model incorporating subducting slabs. *J. geophys. Res. Solid Earth*, **124**, 11549–11567..
- Lu, C., Forte, A.M., Simmons, N.A., Lai, H., Garnero, E.J. & Grand, S.P., 2020. The sensitivity of joint inversions of seismic and geodynamic data to mantle viscosity, *Geochem. Geophys. Geosyst.*, **21**, e2019GC008648.
- Love, A.E.H., 1927. *A Treatise on the Theory of Elasticity*, Cambridge Univ. Press, New York.
- Ma, Z. & Masters, G., 2014. A new global Rayleigh- and Love-wave group velocity dataset for constraining lithosphere properties, *Bull. seism. Soc. Am.*, **104**, 2007–2026.
- Ma, Z., Masters, G., Laske, G. & Pasquano, M.E., 2014. A comprehensive dispersion model of surface wave phase and group velocity, *Geophys. J. Int.*, **199**, 113–135.
- Maggi, A., Tape, C., Chen, M., Chao, D. & Tromp, J., 2009. An automated time-window selection algorithm for seismic tomography. *Geophys. J. Int.*, **178**(1), 257–281.
- Mjelde, R., Eckhoff, I., Solbakken, S., Kodaira, S., Shimamura, H., Gunnarsson, K., Nakanishi, A. & Shiobara, H., 2007. Gravity and S-wave modelling across the Jan Mayen Ridge, North Atlantic; implications for crustal lithology. *Mar. Geophys. Res.*, **28**, 27–41.
- Montagner, J.-P. & Anderson, D.L., 1989. Petrological constraints on seismic anisotropy, *Phys. Earth planet. Inter.*, **54**(1–2), 82–105.
- Moulik, P. & Ekström, G., 2014. An anisotropic shear velocity model of the Earth's mantle using normal modes, body waves, surface waves and long-period waveforms, *Geophys. J. Int.*, **199**, 1713–1738.
- Myers, S.C., Johannesson, G. & Hanley, W., 2007. A Bayesian hierarchical method for multiple-event seismic location. *Geophys. J. Int.*, **171**, 1049–1063.
- Myers, S.C., Johannesson, G. & Hanley, W., 2009. Incorporation of probabilistic seismic phase labels into a Bayesian multiple-event seismic locator. *Geophys. J. Int.*, **177**, 193–204.
- Myers, S.C., Johannesson, G. & Simmons, N.A., 2011. Global-scale P wave tomography optimized for prediction of teleseismic and regional travel times for Middle East events: 1. Data set development. *J. geophys. Res.*, **116**, doi: 10.1029/2010JB007967.

- Myers, S.C., Simmons, N.A., Johannesson, G. & Matzel, E., 2015. Improved regional and teleseismic P-wave travel time prediction and event location using a global, 3-dimensional velocity model, *Bull. seism. Soc. Am.*, **105**(3), 1642–1660.
- Myers, S.C., Ford, S.R., Mellors, R.J., Baker, S. & Ichinose, G.A., 2018. Absolute locations of the North Korean nuclear tests based on differential seismic arrival times and InSAR. *Seismol. Res. Lett.*, **89**(6), 2049–2058.
- Nakiboglu, S.M., 1982. Hydrostatic theory of the Earth and its mechanical implications, *Phys. Earth planet. Inter.*, **28**, 302–311.
- Paige, C.C. & Saunders, M.A., 1982. LSQR: an algorithm for sparse linear equations and sparse least squares, *ACM Trans. Math. Soft.*, **8**, 43–71 and 195–209.
- Panning, M. & Romanowicz, B.a., 2006. A three-dimensional radially anisotropic model of shear velocity in the whole mantle, *Geophys. J. Int.*, **167**(1), 361–379.
- Panning, M.P., Lekić, V. & Romanowicz, B., 2010. Importance of crustal corrections in the development of a new global model of radial anisotropy, *J. geophys. Res.*, **115**, B12325, doi:10.1029/2010JB007520.
- Pasyanos, M.E., Masters, T.G., Laske, G. & Ma, Z., 2014. LITHO1.0: an updated crust and lithospheric model of the Earth, *J. geophys. Res.*, **119**, 2153–2173.
- Ritsema, J. & Van Heijst, H.-J., 2002. Constraints on the correlation of P- and S-wave velocity heterogeneity in the mantle from P, PP, PPP and PKPab traveltimes, *Geophys. J. Int.*, **149**(2), 482–489.
- Ritsema, J. & Lekic, V., 2020. Heterogeneity of seismic wave velocity in Earth's mantle, *Ann. Rev. Earth Planet.*, **48**, 377–401.
- Romanowicz, B., 2003. Global mantle tomography: progress status in the past 10 years, *An. Rev. Earth Planet Sci.*, **31**, 303–328.
- Sambridge, M. & Falettič, R., 2003. Adaptive whole Earth tomography, *Geochem. Geophys. Geosys.*, **4**(3), doi:10.1029/2001GC000213.
- Schuberth, B.S.A., Bunge, H.-P. & Ritsema, J., 2009. Tomographic filtering of high-resolution mantle circulation models: can seismic heterogeneity be explained by temperature alone? *Geochem. Geophys. Geosys.*, **10**, Q05W03, doi:10.1029/2009GC002401.
- Shen, W. & Ritzwoller, M.H., 2016. Crustal and uppermost mantle structure beneath the United States, *J. geophys. Res.*, **121**, 4306–4342.
- Sieminski, A., Liu, Q.Y., Trampert, J. & Tromp, J., 2007. Finite-frequency sensitivity of body waves to anisotropy based upon adjoint methods, *Geophys. J. Int.*, **171**(1), 368–389.
- Simmons, N.A., Forte, A.M. & Grand, S.P., 2007. Thermochemical structure and dynamics of the African superplume. *Geophys. Res. Lett.*, **34**, doi: 10.1029/2006gl028009.
- Simmons, N.A., Forte, A., Boschi, L. & Grand, S.P., 2010. GyPSuM: a joint tomographic model of mantle density and seismic wave speeds, *J. geophys. Res.*, **115**, B12310, doi:10.1029/2010JB007631.
- Simmons, N.A., Myers, S.C. & Johannesson, G., 2011. Global-scale P wave tomography optimized for prediction of teleseismic and regional travel times for Middle East events: 2. Tomographic inversion, *J. geophys. Res.*, **116**, B04305, doi:10.1029/2010JB007969.
- Simmons, N.A., Myers, S.C., Johannesson, G. & Matzel, E., 2012. LLNL-G3Dv3: global P wave tomography model for improved regional and teleseismic travel time prediction, *J. geophys. Res.*, **117**, B10302, doi:10.1029/2012JB009525.
- Simmons, N.A., Myers, S.C., Johannesson, G., Matzel, E. & Grand, S.P., 2015. Evidence for long-lived subduction of an ancient tectonic plate beneath the southern Indian Ocean, *Geophys. Res. Lett.*, **42**, 9270–9278.
- Simmons, N.A., Schuberth, B.S.A., Myers, S.C. & Knapp, D.R., 2019. Resolution and covariance of the LLNL-G3D-JPS Global Seismic Tomography Model: applications to travel time uncertainty and tomographic filtering of geodynamic models, *Geophys. J. Int.*, **217**, 1543–1557.
- Tao, K., Grand, S.P. & Niu, F., 2018. Seismic structure of the upper mantle beneath eastern Asia from full waveform seismic tomography. *Geochem. Geophys. Geosyst.*, **19**, 2732–2763.
- Tesoniero, A., Auer, L., Boschi, L. & Cammarano, F., 2015. Hydration of marginal basins and compositional variations within the continental lithospheric mantle inferred from a new global model of shear and compressional velocity, *J. geophys. Res. Solid Earth*, **120**, 7789–7813.
- Thomsen, L., 1986. Weak elastic anisotropy, *Geophysics*, **51**(10), doi:10.1190/1.1442051.
- Toyokuni, G., Matsuno, T. & Zhao, D., 2020. P-wave tomography beneath Greenland and surrounding regions-II. Lower mantle, *J. geophys. Res. Solid Earth*, doi:10.1002/essoar.10502596.1.
- Tromp, J., Tape, C. & Liu, Q., 2005. Seismic tomography, adjoint methods, time reversal and banana-doughnut kernels, *Geophys. J. Int.*, **160**(1), 195–216.
- Tromp, J., 2019. Seismic wavefield imaging of Earth's interior across the scales, *Nat. Rev.*, **1**, 40–53.
- van der Hilst, R.D., Widjiantoro, S. & Engdahl, E.R., 1997. Evidence for deep mantle circulation from global tomography, *Nature*, **386**, 578–584.
- Visser, K., Trampert, J., Lebedev, S. & Kennett, B.L.N., 2008. Probability of radial anisotropy in the deep mantle, *Earth planet. Sci. Lett.*, **270**, 241–250.
- Yuan, H., French, S., Cupillard, P. & Romanowicz, B., 2014. Lithospheric expression of geological units in central and eastern North America from full waveform tomography, *Earth planet. Sci. Lett.*, **402**, 176–186.
- Zhao, D., Hasegawa, A. & Horiuchi, S., 1992. Tomographic imaging of P-waves and S-wave velocity structure beneath northeastern Japan, *J. geophys. Res.*, **97**, 19909–19928.
- Zhao, D., Yamamoto, Y. & Yanada, T., 2013. Global mantle heterogeneity and its influence on teleseismic regional tomography, *Gondwana Res.*, **23**, 595–616.
- Zhao, D., 2015. *Multiscale Seismic Tomography*. Springer, pp. 304.
- Zheng, Y. & Lay, T., 2006. Low Vp/Vs ratios in the crust and upper mantle beneath the Sea of Okhotsk inferred from teleseismic pMP, sMP, and sMS underside reflections from the Moho, *J. geophys. Res.: Solid Earth*, **111**, doi: 10.1029/2005JB003724.
- Zhou, T., Chen, M., Xi, Z. & Li, J., 2021. Initial model assessment for intermediate-period full-waveform inversion of the contiguous U.S. and surrounding regions, *Geophys. J. Int.* (submitted), doi: 10.31223/X5V599.
- Zucca, J.J. et al., 2009. The prospect of using three-dimensional Earth models to improve nuclear explosion monitoring and ground motion hazard assessment, *Seismol. Res. Lett.*, **80**, 31–39.

## SUPPORTING INFORMATION

Supplementary data are available at *GJI* online.

**Text S1:** P-wave traveltimes event selection.

**Text S2:** Bayesloc multiple-event relocation.

**Text S3:** 3-D ray tracing.

**Text S4:** Surface wave sensitivities and velocity calculations.

**Text S5:** Additional inversion details.

**Figure S1:** Body wave hit count in the lower mantle.

**Figure S2:** Body wave hit count in the crust and upper mantle.

**Figure S3:** Body wave hit count in high-resolution zones.

**Figure S4:** Example surface wave velocity maps.

**Figure S5:** L-curve analysis.

**Figure S6:** Regional body wave fit improvement in high-resolution zones.

**Figure S7:** Waveform simulations for 2008 Wells earthquake for station A16A.

**Figure S8:** Waveform simulations for 2005 Qeshm earthquake for station ANTO.

**Figure S9:** Waveform simulations for DPRK6 declared nuclear test for station KNP.

**Figure S10:** Rayleigh wave dispersion tests beneath the Pacific Ocean.

Please note: Oxford University Press is not responsible for the content or functionality of any supporting materials supplied by the authors. Any queries (other than missing material) should be directed to the corresponding author for the paper.